Ionics and electrodics of oxides with fluorite-related structures for proton-conducting solid oxide fuel cells

Vasileios Besikiotis

Dissertation for the degree
of Philosophiae Doctor

Department of Chemistry
Faculty of Mathematics and Natural Sciences
University of Oslo

2013

Series of dissertations submitted to the
Faculty of Mathematics and Natural Sciences, University of Oslo
No. 1324

ISSN 1501-7710

Cover: Inger Sandved Anfinsen.
Printed in Norway: AIT Oslo AS.

Produced in co-operation with Akademika publishing.
The thesis is produced by Akademika publishing merely in connection with the thesis defence. Kindly direct all inquiries regarding the thesis to the copyright holder or the unit which grants the doctorate.

Preface

The present thesis is the summation of the work that I have carried out for the degree of Philosophiae Doctor (PhD) at the Faculty of Mathematics and Natural Sciences, University of Oslo. The work has been conducted in the research group for Solid-State Electrochemistry led by Prof. Truls Norby, Department of Chemistry, funded by the European Union, FP7 "EFFIPRO" project (grant agreement no. 227560), in the period from May 2009 to June 2012.

The completion of this work would have been *impossible* without the *aid* and *support* of many, as expressed in the *"Acknowledgements"* at the end of this thesis. Nevertheless I would like to dedicate this work to *Siri*, for her endless support and patience all these years, and especially these last months.

Oslo, December 2012

Vasileios Besikiotis

Contents

Publications during PhD not included in this thesis:

- N. Kaklidis, V. Besikiotis, G. Pekridis, G.E. Marnellos "Acetic acid internal reforming in a solid oxide fuel cell-reactor using Cu-CeO_2 anodic composite", *International Journal of Hydrogen Energy*, **37 (21)**, p. 16722-16732 (2012)

- N. Kaklidis, G. Pekridis ,V. Besikiotis, C. Athanasiou, G.E. Marnellos "Direct electro-oxidation of acetic acid in a solid oxide fuel cell", *Solid State Ionics*, **225**, p.398-407 (2012)

- P.D.C. Dietzel, V. Besikiotis, R. Blom "Application of metal-organic frameworks with coordinatively unsaturated metal sites in storage and separation of methane and carbon dioxide", *Journal of Materials Chemistry*, **39**, p. 7362-7370 (2009)

1. Introduction

"It is clear that there is some difference between ends: some ends are energia [energy] while others are products which are additional to energia"

Aristotle

Metaphysics Z-H

1.1 Motivation

Ενέργεια (energia)*, ενδελέχεια* (endelechia) and *δύναμη* (dynami) are three terms that Aristotle used in order to describe and argue the essence of *ουσία* (ousia)[1] [1]. He used *energy* to describe something that is *ενεργό* (energo)[2]. In physical chemistry the energy of a system is defined as its capacity to do work [2]. In the context of chemistry, chemical energy is the potential of a substance to undergo a transformation through a chemical reaction or to transform to other chemical substances.

Moreover, energy is playing a dominant role in determining the quality of life, and is the single most important factor that impacts the prosperity of any society. However, approximately a quarter of today's world has access to energy at the level which, for instance, the citizens of Europe have. The world's population will level at around 10 billion people. In order to give everybody the same energy affluence we would need to generate approximately 60 TW of energy. That is four times the amount of energy we need now, and would demand almost 900 million barrels of oil per day [3].

[1] *Energia*, *endelechia*, and *dynami* are the Greek words for energy, entelechy and potency respectively, while *ousia* means substance.
[2] *εν*-at and *εργο*-work; in free translation from Greek to English is "being-at-work".

In order to tackle this challenge what we need, as the chemistry Nobel prize laureate Richard E. Smalley stated in [3], is to find the "new-oil", and to be able to produce energy in a sustainable manner. Production of energy from burning fossil-fuels (oil, gas, and coal) is not efficient. From a thermodynamic point of view, the efficiency of a real heat engine is smaller than that of an ideal Carnot heat engine. In addition, taking into consideration the forecasts for the abundance of fossil-fuels and the environmental footprint of the use of such energy resources, energy production is definitely not sustainable today. Therefore, the development of technologies that can deliver energy efficiently and sustainably is vital.

It is interesting to note that the fundamental knowledge of converting energy from one form to another without being subjected to Carnot limitations, dates back in the late 1830's and early 1840's pioneered by Sir William Grove. In 1842 Grove developed a device that he called gas voltaic battery, where hydrogen was being electrochemically oxidized by oxygen to water, producing electricity [4]. Since then, the advances in science and technology have allowed devices based on the principles described by Grove, namely fuel cells, to supply auxiliary power to NASA's Gemini Program in the 1960's and since 2008 to provide Google's servers with 100 kW [5]. These are only two out of the many examples that can reveal the potential of fuel cells. Yet, two main reasons impede the dominance of such devices in the energy field. The first is the lack of political will for change, but the discussion of this aspect is beyond the scope of this thesis. The second is the development and a deeper understanding of the functional properties of materials that compose such devices, in order to overcome challenges related to high power density output, long life operation, and cost reduction.

Electrochemistry is the field of science that encompasses inter-relations of electrical and chemical phenomena subdivided to *ionics*, dealing with ions in solutions, and *electrodics*, dealing with ions and electrons at the electrode-electrolyte interface. Defect chemistry is the study of deviations from perfect order in crystalline inorganic compounds, and the effects of such disorder on their properties. In this thesis defect chemistry and electrochemistry provide the path for understanding the transport properties and hydration thermodynamics of selected materials, namely disordered fluorite related structures, which can be used as components in proton conducting solid oxide fuel cells.

1.2 Principles of proton conducting solid oxide fuel cells (PC-SOFCs)

A fuel cell is an electrochemical energy converter, which can continuously convert the chemical energy of a fuel (typically hydrogen, H_2) and an oxidant (air) to electrical energy, by a process involving an essentially invariant electrode electrolyte system. PC-SOFCs are such converters, which operate at temperatures around 800 °C, and can use hydrogen as fuel. The architecture of a typical PC-SOFC consists of two electrodes, the anode and the cathode, and a dense electrolyte (cf. Fig.1.1).

In a PC-SOFC the electrolyte is typically a ceramic material *e.g.* acceptor doped $BaCeO_3$, in which protons are neither part of the stoichiometry nor the structure, but introduced from the surrounding environment *i.e.* water or hydrogen, to charge compensate negative defects which are part of the nonstoichiometry or structure. Protons are attached to oxide ions as hydroxide groups forming effectively positive defects, $OH_O^{\bullet}$.

The electrodes of a PC-SOFC are porous structures, in order to facilitate gas transport, exhibiting high electronic conductivity and large electrode-electrolyte-gas triple phase boundary (TPB) length. Moreover, they should reveal good catalytic activity for the oxidation of the fuel (anode) and the reduction of the oxidant (cathode). Typical systems used as electrodes in a PC-SOFC where the electrolyte is acceptor doped $BaCeO_3$, are Ni cermets on the anode side, and mixed electronic ionic conductors (MIECs) such as cobalt ferrites or noble metals such as Pt and Ag, on the cathode side.

The fuel, for instance H_2, is fed to the anode side and oxidized releasing electrons:

$$2H_2(g) \rightarrow 4H^+ + 4e^- \tag{1.1}$$

The released electrons are transported to the cathode via an external circuit (cf. Fig. 1.1). At the cathode, the oxidant (typically air) is reduced consuming the transported electrons and forming water:

$$4H^+ + O_2(g) + 4e^- \rightarrow 2H_2O \tag{1.2}$$

Formation of water at the cathode side prevents the dilution of the fuel with water, resulting in higher fuel efficiency and allowing the operation of the cell at maximum power and preventing the oxidation of the anode, opposed to conventional solid oxide fuel cells (SOFCs) where the electrolyte is an oxide ion conductor. The electrolyte allows the protons to transport through, in order to complete the overall electrochemical reaction:

$$H_2(g) + \tfrac{1}{2}O_2(g) \rightarrow H_2O \tag{1.3}$$

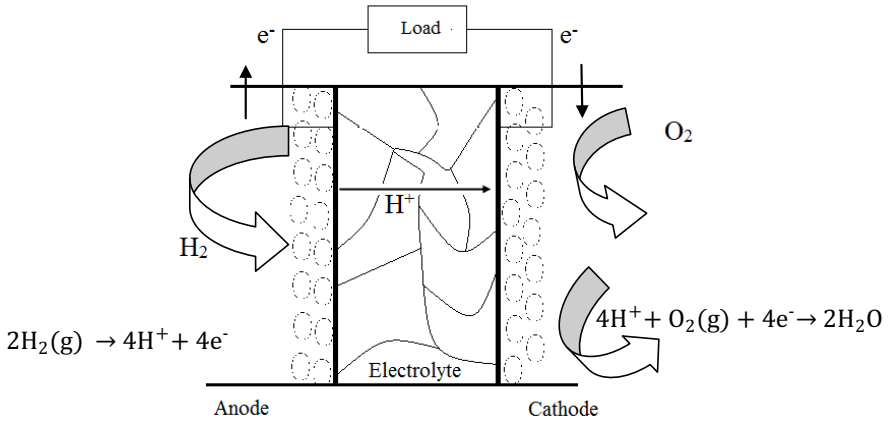

Figure 1.1 Operating principle of a solid oxide fuel cell with a proton conducting electrolyte.

The release of electrons through the external circuit generates direct-current. The electrochemical difference between the anode and the cathode leads to a potential difference across the cell which corresponds to the Gibb's energy ΔG for the oxidation of H_2 (eq. 1.3):

$$\Delta G = -\mathrm{n}FE \tag{1.4}$$

where n is the number of electrons, F is Faraday's constant, and E is the reversible potential of the cell. When the reactants and product of the reaction in eq.1.3 are in their standard state then eq.1.4 is written as:

$$\Delta G^0 = -\mathrm{n}FE^0 \tag{1.5}$$

where ΔG^0 is the standard Gibb's energy of the reaction in eq.1.3, and E^0 is the standard potential of the cell.

In a PC-SOFC at temperature T the ΔG of the cell reaction in eq. 1.3 is calculated through:

$$\Delta G = \Delta G^0 + RT\ln\left(\frac{\sqrt{pO_2}pH_2}{pH_2O}\right) \tag{1.6}$$

so that the reversible potential is given by:

$$E = -\frac{\Delta G^0}{nF} + \frac{RT}{nF}\ln\left(\frac{\sqrt{pO_2}pH_2}{pH_2O}\right) \tag{1.7}$$

where p is the partial pressure of the reacting species and R is the gas constant. Eq.1.7 quantifies the relationship between the standard and reversible potential for the electrochemical reaction of a PC-SOFC.

The actual cell voltage is smaller than the reversible potential because of irreversible losses, so-called overpotentials. Losses originate either from the potential requirements to activate electrochemical reactions, the activation overpotential $-\eta_{act}$, ohmic losses, ohmic overpotential $-\eta_{ohm}$, and/or from losses due to the mass transport of species participating to the electrochemical reactions, concentration overpotential $-\eta_{conc}$. The sum of all above mentioned losses is the total overpotential or polarization of the cell, η, given by the difference between the operating cell voltage, E_{op}, and the expected reversible cell voltage, E, $\eta = E_{op} - E$. The effect of each overpotential can be seen in the polarization curve presented in Fig. 1.2. The aim of this work is to investigate materials that can contribute to reduce these overpotentials.

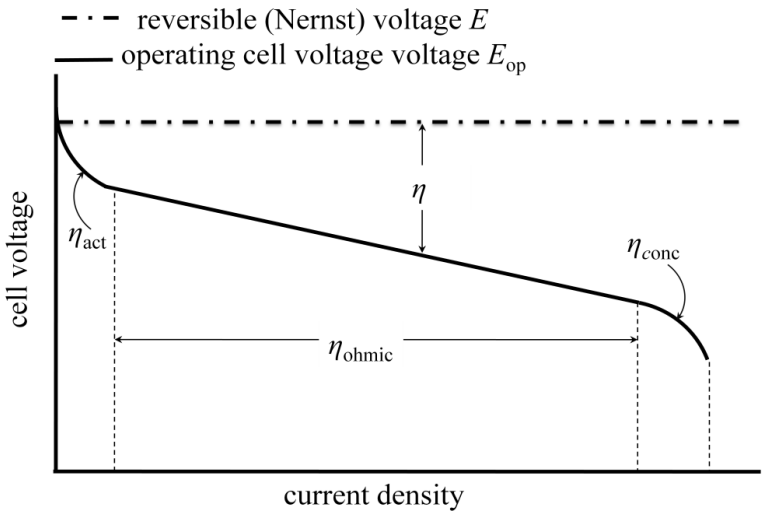

Figure 1.2 Schematic polarization curve of a fuel cell.

1.3 Materials challenges

Despite the promising characteristics of PC-SOFCs, their current status is still quite far from broad commercialization. From technological prospective the applicability of state-of-the-art proton conductors such as acceptor doped $BaCeO_3$, $SrCeO_3$, $BaZrO_3$ as electrolytes, is hampered by their high grain boundary resistivity and poor stability. Due to their basic nature, as Sr and Ba are the main components, they are vulnerable to acidic environments *e.g.* CO_2 and SO_2, and steam that may be present during operation.

Regardless of the deep level of understanding of transport and thermodynamic mechanisms governing proton conductivity in state-of-the-art electrolytes, research on electrodes is somewhat less extensive. On the anode side, Ni cermet, composed from NiO and the proton conducting electrolyte, is the most preferable system for anodes due to its excellent electrocatalytic activity towards H_2 oxidation. However during production and operation the most commonly used electrolyte $BaCeO_3$ reacts with NiO-Ni, destroying the electronic conductivity of the anode and reducing the proton transport number of the electrolyte.

On the cathode side, water formation results a plethora of co-existent charge carriers making the cathode reactions more complex. It is common in PC-SOFC demonstrations the use of Pt or Ag, as cathodes. These are primarily expensive metals and given their pure electronic character they exhibit inadequate performance. Hence, research has also been focused on the development of electrodes with mixed oxygen ion-electron conductors, as in the case of solid oxide fuel cells (SOFCs), in order to promote the oxygen reduction on the cathode side [6-9], cf. Fig.1.1. Yet, using mixed oxygen ion-electron conducting cathodes restricts water formation at the cathode / electrolyte interface resulting in slow reaction kinetics [9, 10], and possibly delamination of the cathode caused by water accumulation at the cathode / electrolyte interface. Oxides with mixed ionic (proton and oxide ion)-electronic conductivity as cathodes, are expected to favour the cathode reaction by assisting the oxygen reduction and by delocalizing water formation from the cathode / electrolyte interface to the whole surface area of the cathode.

1.4 Aim of this thesis

As described in the preceding section, there is a need for exploration beyond the state-of-the-art acceptor doped perovskites, both to bring PC-SOFCs closer to commercialization and to broaden the scientific knowledge and understanding. This work explores and attempts to gain knowledge on the electrical properties and hydration thermodynamics of oxides with disordered fluorite related structures − knowledge that can be utilized and implemented in the design of technologies that exploit mixed ionic electronic conduction, as in the case of PC-SOFCs.

The first manuscript is on the hydration thermodynamics of rare earth pyrochlore structured oxides, while the second and the third manuscripts concern the hydration and transport properties of disordered fluorites. In the second manuscript we also emphasized on the determination of the crystal structure of lanthanum cerate. Furthermore, recent advances have shown that lanthanum tungstate is a promising electrolyte for PC-SOFCs. The fourth manuscript is based on the development of cathodes for lanthanum tungstate. Before presenting the four manuscripts a theory part is introduced, where theoretical and conceptual aspects on the structure, ionic transport, hydration thermodynamics and electrodes are discussed; that are considered cumbersome for the inclusion in the manuscripts and with the intention to introduce the reader to the basic complementary

knowledge needed for the manuscripts. Consequently, given the broadness of the topic it is natural to split the theory part into two chapters, chapter 2 and 3. Chapter 2 discusses phenomenological and conceptual aspects on ionics and chapter 3 on electrodics. The thesis is finalized with a discussion on the grain boundary conductivity of lanthanum cerate. Moreover an Appendix is included summarizing the EFFIPRO project and reporting the contribution of the different partners on the anode development for lanthanum tungstate.

No theory on the experimental techniques themselves is included, primarily because this is beyond the scope of this thesis, and it would have been a superficial repetition of what one can find in relevant textbooks. Exception is the density functional theory (DFT) part that is included in chapter 2.

2. Phenomenological aspects and concepts of ionics

2.1 On structure and disorder

"Everything that depends on the action of nature is by nature as good as it can be"

Aristotle

Nicomachean Ethics, 356 B.C

The crystal structure of fluorites and pyrochlores is similar. In order to assist the reader with manuscript I-III, this subchapter begins with a description of the crystallography of the compounds considered in this thesis, how they are crystallographically related, and continues with a rudimentary discussion on structural disorder.

2.1.1 Crystallography.

Oxides, XO_2, adopting the fluorite structure, crystallize in the space group *Fm-3m*. Fig. 2.1 shows the unit cell of the fluorite structure. Going from the fluorite structure to the rare earth (RE) containing pyrochlore $RE_2X_2O_6O'$ the cation and anion ratio is decreasing

[11], and one of the oxide ion positions of the fluorite structure is now adjacent to the cation sublattice exhibiting an alternating REXREX pattern. This results in doubling of the cubic cell lattice parameter from approximately 5 Å to 10 Å [11].

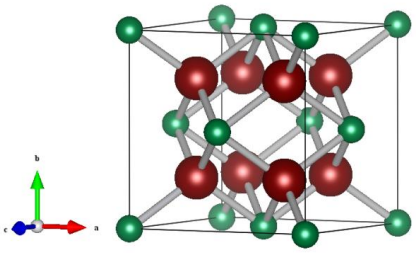

Figure 2.1 Schematic representation of the fluorite unit cell of XO_2, smaller green spheres are X^{4+}, larger red are O^{2-}. The size of the spheres is analogous to the ionic radii of Zr^{4+} and O^{2-} [12].

In this respect a pyrochlore is a fluorite derivative superstructure, with a cubic symmetry crystallizing in the *Fd-3m* space group. Crystallographically there are four unique atom positions. A common way of describing the structure is by fixing its origin on the X site, with atoms located at the following positions (using Wyckoff notation): RE at 16*d*, X at 16*c*, O at 48*f* (O48f), and O' at 8*b* (O8b) [13] and one unoccupied interstitial site at 8*a* (v_{i8a}). The RE site is 8 fold coordinated and the X site is 6 fold coordinated. The two oxygen sites are coordination-wise non-equivalent. The O48f sites are located in the XO_6 octahedron, and thus coordinated to both the RE and X site cations, while the O8b sites are only coordinated to the RE cations. Similarly, the unoccupied v_{i8a} sites are coordinated only to the X site cation, Fig. 2.2 is a colored visualization of Fig. 1b in manuscript II showing 1/8 pyrochlore unit cell and, highlighting the coordination of the different ions as well as their respective site occupancy. Nevertheless the illustration in Fig. 2.2 represents an idealized situation. In reality the change in the cation radius ratio will introduce a rearrangement of the anions around the 8*a* site.

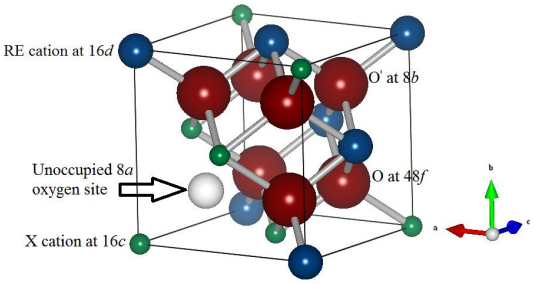

Figure 2.2 Schematic representation [12] of site occupancy and coordination of cations RE^{3+} (medium blue) and X^{4+} (small green), oxygen anions (large red) and the unoccupied 8*a* site (white) into the 1/8 pyrochlore unit cell.

In a disordered fluorite with the stoichiometry $RE_2X_2O_7$, *i.e.* $La_2Ce_2O_7$, space group *Fm-3m*, cations do not reside on specific positions; rather they are randomly orientated in the cation sublattice. Oxygen anions are also randomly orientated with 7/8 occupancy (cf. Fig. 1a manuscript II).

2.1.2 Structural disorder

There are different ways in which disorder can perturb the order into crystalline solids, such as imperfections in position, composition and electronic state. Structural disorder occurs easily in pyrochlores because the enthalpy difference between fluorite and pyrochlore is often rather small. This disorder, which can be considered as a partial reversion of the pyrochlore back towards fluorite, may occur on a scale of either atoms or tens of nanometres [14]. This thesis is concerned with structural disorder in cerate-zirconate systems, as this is described by the cation radii ratio, when moving from the disordered fluorite to the pyrochlore. The stability field of the pyrochlore structure for zirconates has been established in the range $1.46 \leq r_{RE^{3+}}/r_{X^{4+}} \leq 1.80$ [14, 15]. The decrease or increase of $r_{RE^{3+}}/r_{X^{4+}}$ ratio reflects upon the so-called oxygen position parameter *x*, as a result of the distortion of the XO_6 octahedron and the REO_8 cube [16].

All ions in the pyrochlore structure have their positions fixed by symmetry except the O48f. The *x* takes into account the amount that O48f moves away from the centre of its

coordination tetrahedron towards the empty 8*a* site. The value of *x* is a function of the cation radii. Large $r_{RE^{3+}}/r_{X^{4+}}$ ratios lead to large *x*, as in the case of pyrochlores, and vice versa [14]. Therefore, in order to qualitatively express the degree of the cation order in the cerate-zirconate series of materials, we defined an empirical cation order factor φ as a qualitative indicator of the disorder, given by:

$$\varphi = \left(\frac{r_{RE^{3+}}}{r_{X^{4+}}} - 1.33\right) \cdot 3.57 \tag{2.1}$$

The factor $\varphi\ (0 \leq \varphi \leq 1)$ is based on the ratio of the radii between RE (8 fold coordinated) and X (6 fold coordinated) cations, $r_{Ln^{3+}}$ and $r_{X^{4+}}$ are the Shannon radii of RE and X cations in $RE_2X_2O_7$ (X = Ce, Zr). When φ is 0 the system is fully disordered and when φ is 1 it is fully ordered. Intermediate values of φ indicate the degree in which the reversion of the pyrochlore back and towards fluorite occurs. However, a fundamental assumption in this parameterization of cation disorder is that the same trend in cation disorder follows in quaternary systems as $La_2(Ce_{1-x}Zr_x)O_7$, and $r_{X^{4+}}$ is the composition weighted average defined as: $r_{X^{4+}} = x \cdot r_{X^{4+}} + (1 - x) \cdot r_{X^{4+}}$. Fig. 2.3 shows the transition from one structure to the other as a function of φ and $r_{RE^{3+}}/r_{X^{4+}}$. For the studied systems that lie close to the edge of the stability field between disordered fluorite and pyrochlore, structural disorder occurs easily because the enthalpy difference between pyrochlores and disordered fluorites is often rather small [14, 17, 18].

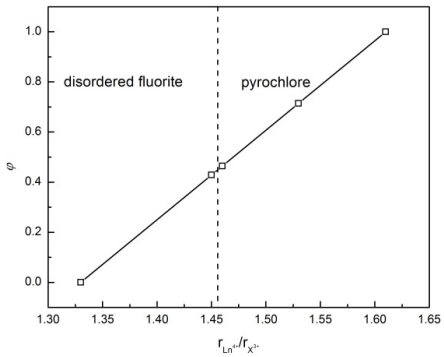

Figure 2.3 Cation order factor *φ vs.* cation radii ratio for the systems studied in this work.

The treatment of the oxygen position parameter x is beyond the scope of this work and none of the experimental techniques used in this thesis is suitable for the accurate determination of x. Yet, the importance of inclusion of x into eq.2.1 is acknowledged, as this parameter has an essential effect on the structural features of the system. Especially if one defines an order or tolerance factor that is generic for the whole pyrochlore family, as in the study of Cai *et al.* [16].

2.2 Ionics of disordered fluorite related structures

ιόν (e-on)-ion, in ancient Greek is the meaning of going

This subchapter contains additional and more detailed theory than what could be included in manuscripts I-III. The main materials' property that determines the suitability of a disordered fluorite as a potential electrolyte for a PC-SOFC is the proton conductivity. A prerequisite for proton transport in a crystalline solid are defects. In a broader sense, any deviation from the reference state, that is the ideal structure, is termed a defect [19]. In this thesis the focus is on proton and oxide ion point defects.

A main characteristic of disordered fluorite related oxides is that protons are not part of their structure, rather they are introduced into the structure from the surrounding environment *i.e.* water in this work. I therefore start my treatment with describing how defects form, and prior to transport mechanisms I introduce some of the thermodynamic concepts that have been used in the manuscripts.

2.2.1 On the defect chemistry of disordered fluorites and pyrochlores

Point defects consist of vacancies and interstitial atoms. Impurity atoms are also termed point defects, whether they occupy a structural or an interstitial site. Point defects can be formed with or without the reaction of the surrounding environment, termed as external and internal defect reactions, respectively. A proton, stems from the ionization of hydrogen. This proton will be located in the electron cloud of an oxide ion, such that the species is a hydroxide ion on the site of an oxide ion, being effectively positive, $OH_O^{\bullet}$ [20].

When a charged point defect is formed in an oxide[3] a balancing point defect with opposite effective charge must be formed to preserve the electroneutrality. In metal oxides two types of internal defect equilibria involving point defects have been found to be important, the Schottky and Frenkel disorder. In pyrochlore systems computational studies [17, 21, 22] have shown that anti-Frenkel[4] disorder consisting of a pair of an oxygen vacancy, $v_O^{\bullet\bullet}$, and an oxygen interstitial, $O_i^{//}$, is the most favourable disorder mechanism. Considering the crystallography of pyrochlores as discussed in subchapter 2.1, anti-Frenkel pair defect formation is considered at all oxygen sites *i.e.* $v_{O8b}^{\bullet\bullet}$, $v_{O48f}^{\bullet\bullet}$, $O_{i8a}^{//}$. Then the anti-Frenkel pair defect formation may read as:

$$O_{O48f}^{x} + v_{i8a}^{x} = v_{O48f}^{\bullet\bullet} + O_{i8a}^{//} \tag{2.2}$$

or

$$O_{O8b}^{x} + v_{i8a}^{x} = v_{O8b}^{\bullet\bullet} + O_{i8a}^{//} \tag{2.3}$$

As we show and discuss in manuscript I, defect formation for pyrochlores is favoured through eq.2.2. On the other hand, as cation disorder increases by increasing the size of the X cation and the structure of disordered fluorite is adopted, formation of $v_{O8b}^{\bullet\bullet}$, is equally favored.

Given the crystallography of pyrochlores, proton formation is also expected to happen at all oxygen sites *i.e.* $OH_{O48f}^{\bullet}$, $OH_{O8b}^{\bullet}$, $OH_{O8a}^{/}$. Fig. 2.4 illustrates possible configurations of a proton on the O8b and O48f ions into five *sites* termed *a-e* within $RE_2X_2O_7$[5]. According to DFT calculations[6] the most stable proton position for pyrochlores is close to the O48f ion in *site a* (96g symmetry), while for disordered fluorites protons can also be stabilized close to the O8b ion.

[3] Deliberately the distinction between *stoichiometric* and *nonstoichiometric* compositions is avoided, since stoichiometric composition in inorganic compounds is in principle the exception rather than the rule. Oxides in equilibrium with their surroundings are thus generally nonstoichiometric, except under specific conditions of temperature and activities.
[4] Ant-Frenkel disorder consists of anion point defects while Frenkel consists of cation point defects.
[5] The figure was generated from structural data for $La_2Sn_2O_7$
[6] In subchapter 2.3 the computational formalism for these calculations is provided.

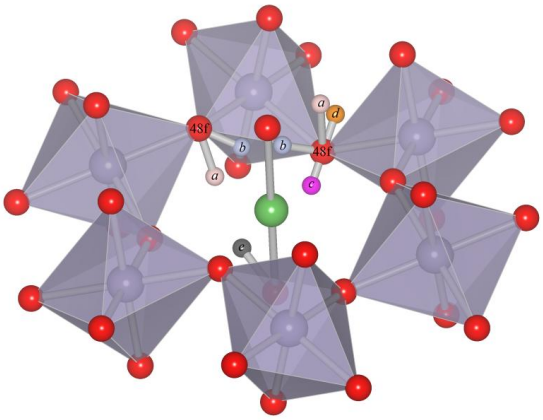

Figure 2.4 Proton sites in $RE_2X_2O_7$ pyrochlore. Sites *a-d* are coordinated to O48f and the *e* site is bonded to an O8b. The green and violet spheres are the RE^{3+} and X^{4+} cations, respectively.

The most prominent effect of the transition from pyrochlore to disordered fluorite is the occupation of both the two interstitial defects, O''_{i8a} and OH'_{i8a}, and the two defects at the O8b site, $OH^{\bullet}_{O8b}$ and $v^{\bullet\bullet}_{O8b}$. Hence, while such defects are in complete minority in ordered pyrochlores, their concentration is significantly increasing as part of the increasing disorder. Consequently, in systems with large values of φ (manuscript III) or more generally large values of $r_{RE^{3+}}/r_{X^{4+}}$, defect formation mainly occurs on the O48f site, whereas systems with more similar cations, and therefore higher degree of cation disorder, also display a large degree of anion disorder among the different oxygen sites. Thus in cerates, for instance, the occupation of the different oxygen sites is close to indistinguishable.

2.2.2 Hydration thermodynamics

As we discussed in the preceding paragraph the formation of $v_{O48f}^{\bullet\bullet}$ is favoured in both pyrochlores and disordered fluorites. These oxygen vacancies in their dry state[7] may interact with water vapour according to:

$$H_2O(g) + v_{O48f}^{\bullet\bullet} + O_O^{\times} = 2OH_{O48f}^{\bullet} \quad (2.4)$$

When reaction 2.4 proceeds in the forward direction, the annihilation of $v_{O48f}^{\bullet\bullet}$ is followed by the formation of two $OH_{O48f}^{\bullet}$, and the requirement for charge balance is fulfilled. This reaction, normally referred as hydration reaction in the relevant literature, is of great technological interest in the field of PC-SOFCs as it describes the creation of protonic defects. Moreover, as evident from the hydration reaction, the amount of protons that can be incorporated in the system, is limited by the amount of $v_{O48f}^{\bullet\bullet}$ available for hydration. Traditionally a strategy that is commonly adopted for state of the art proton conductors *i.e.* perovskites, is to try to maximize the amount of oxygen vacancies via external doping. Substitution of cations in the host material by a lower valence element, introduces effectively negative point defects. These must be compensated by the creation of an oppositely charged defect, and at moderate oxygen pressures the materials tend to form oxygen vacancies. This type of aliovalent substitution is termed acceptor doping [23]. As we show in manuscript I, acceptor doping of ordered pyrochlores favours the formation of $v_{O48f}^{\bullet\bullet}$, and the maximum of the proton concentration that can be achieved is defined by the acceptor doping level, $[Acc']$, given by the electroneutrality:

$$[Acc'] = 2[v_{O48f}^{\bullet\bullet}] + [OH_{O48f}^{\bullet}] \quad (2.5)$$

The mass action expression for the equilibrium constant for the hydration reaction reads:

$$K_{hydr} = \frac{\left(\frac{[OH_{O48f}^{\bullet}]}{N_{s,OH_{O48f}^{\bullet}} N_{c,OH_{O48f}^{\bullet}}}\right)^2}{\frac{[v_{O48f}^{\bullet\bullet}]}{N_{s,v_{O48f}^{\bullet\bullet}} N_{c,v_{O48f}^{\bullet\bullet}}} \frac{[O_O^{\times}]}{N_{s,O_O^{\times}}} \frac{p_{H_2O}}{p^0}} = \exp\left(-\frac{\Delta_{hydr}G^0}{RT}\right) =$$

$$\exp\left(\frac{\Delta_{hydr}S^0}{R}\right) \exp\left(-\frac{\Delta_{hydr}H^0}{RT}\right) \quad (2.6)$$

[7]In principle, protons may be incorporated directly as charge compensating defects in the presence of water *e.g.* ambient humidity, during synthesis. Yet, synthesis, annealing and sintering are usually done at rather elevated temperatures where protons are minority.

where $N_{s,i}$ and $N_{c,i}$ are the concentration of sites and number of configurations per site, respectively, $\Delta_{hydr}G^0$ is the Gibbs energy of the reaction, and $\Delta_{hydr}S^0$ and $\Delta_{hydr}H^0$ are the standard entropy and enthalpy of the hydration reaction. Empirically the expected standard entropy change from the loss of one gas molecule per unit reaction is in the order of -120 J·mol^{-1}·K^{-1} [24] and this value is typically set as an initial estimate for $\Delta_{hydr}S^0$. Consequently the hydration reaction is an exothermic reaction favoured for negative values of $\Delta_{hydr}H^0$ (cf. Fig. 2.5) for the conditions considered here.

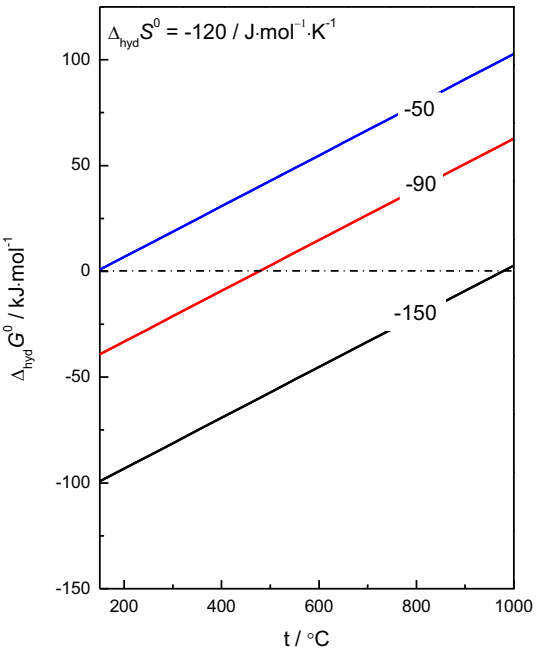

Figure 2.5. Change of $\Delta_{hydr}G^0$ with temperature for varying $\Delta_{hydr}H^0$ in kJ·mol^{-1} and unvarying $\Delta_{hydr}S^0$.

Moreover, Fig. 2.6 shows the variation in proton and oxygen vacancy concentration for a 10 mol% acceptor doped ordered pyrochlore, as a function of inverse temperature with varying the hydration enthalpy and keeping constant the hydration entropy. In a system with a more exothermic hydration enthalpy, protons dominate as the main charge compensating defects up to higher temperatures, compared to a system with less

exothermic hydration enthalpy. It is further illustrated that the temperature at which the majority of protonic defects changes to oxygen vacancies exclusively depends on the hydration enthalpy, when the hydration entropy is kept constant. This observation highlights the importance of hydration enthalpy as a parameter for the transport properties of a system.

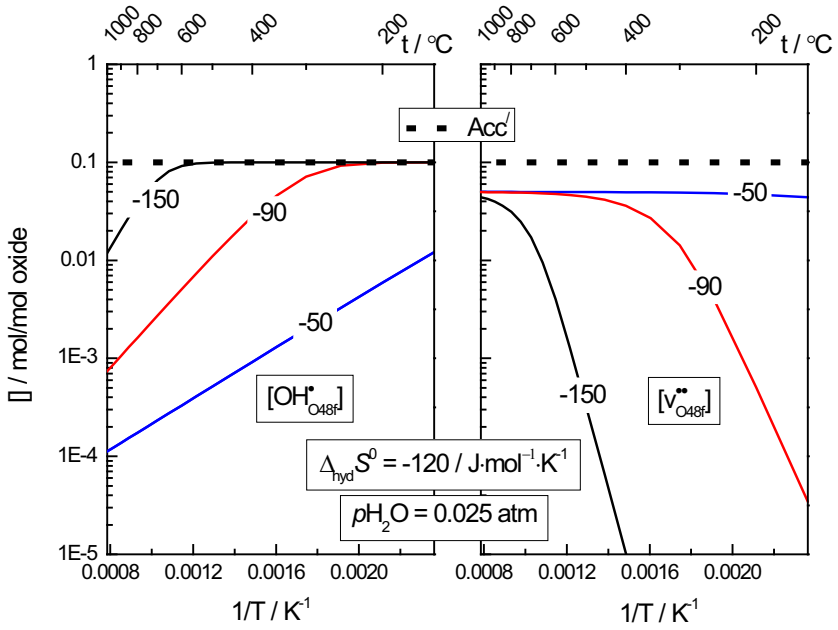

Figure 2.6. Idealized temperature dependency of $OH^{\bullet}_{O48f}$ and $v^{\bullet\bullet}_{O48f}$ concentrations for a 10 mol% acceptor doped ordered pyrochlore, pH_2O=0.025 atm, with varying $\Delta_{hydr}H^0$ (kJ·mol^{-1}) and constant $\Delta_{hydr}S^0$.

Moreover, in manuscript I, we show that the formation of oxygen vacancies on the 8b site is favoured and compensated with an oxygen interstitial on the 8a site, when substituting the X-site in $RE_2X_2O_7$ with a larger ion; as in the case of $Sm_2X_2O_7$ with X = Ce and Ti. Then the electroneutrality condition reads:

$$2\left[O''_{i8a}\right] = 2[v^{\bullet\bullet}_{O48f}] + 2[v^{\bullet\bullet}_{O8b}] + [OH^{\bullet}_{O48f}] + [OH^{\bullet}_{O8b}] \qquad (2.7)$$

Based on eq. 2.7 one would expect that for systems such as cerates that possess high degree of disorder, hydration would be more favourable than for *e.g.* zirconates. Yet, in manuscript III, we show that the hydration enthalpy as a function of x within $La_2(Ce_{1-x}Zr_x)_2O_7$ (x = 0 to 1) follows a volcano like behaviour, where the highly disordered

$La_2Ce_2O_7$ reveals as favourable hydration thermodynamics as the fully ordered $La_2Zr_2O_7$. We attribute this behaviour to the gradual increase in the stability of the oxygen vacancies as order increases with increasing Zr content, and to changes in the coordination number and bonding nature that would favour the hydration thermodynamics once the ordered pyrochlore structure is attained. Furthermore, our findings in manuscript I revealed that the hydration enthalpy is increasing (less exothermic) with decreasing RE-ion size, attributed to destabilization of protons and stabilization of oxygen vacancies. The effect of order/disorder on the transport properties and hydration thermodynamics is presented in manuscript III.

2.2.3 Transport properties

Once the available oxygen vacancies are hydrated and filled with protons, the transport properties of these defects are of importance. In the following I shall describe the transport mechanisms of these defects, in disordered fluorite related structures, and attempt to rationalize the electrical properties of those structures.

Conductivity

In a solid medium the flow of charged species will give rise to current. In an ionic solid the net motion of charged defects (*e.g.* electrons, impurity ions, dopant ions and protons) will also produce current; what is termed as *conductivity*. The conductivity of a species i in an ionic solid is parameterized through:

$$\sigma_i = z_i e \mathrm{c}_i u_i \tag{2.8}$$

where $z_i e$ is the charge of each particle, c_i is the volume concentration of the species and u_i is the *mobility* of the species. The mobilities of electrons and electron holes are normally much higher than those of ions hence most oxides reveal to some extend electronic conductivity, and the total conductivity, σ_{tot} will be given as the sum of electronic, σ_{el}, plus the ionic, σ_{ion}, conductivity. Depending on the conditions of temperature and oxygen partial pressure, typically one type of charge carrier predominates the total conductivity. For pyrochlores, if we consider the formation of a doubly ionized $\mathrm{v}_{\mathrm{O48f}}^{\bullet\bullet}$ the total reaction may read:

$$O_{O48f}^{x} = v_{O48f}^{\bullet\bullet} + 2e^{/} + \frac{1}{2}O(g) \tag{2.9}$$

$$K_{v_{O48f}^{\bullet\bullet}} = [v_{O48f}^{\bullet\bullet}][e^{/}]^2 p_{O_2}^{\frac{1}{2}} \tag{2.10}$$

with equilibrium constant given by eq. 2.10. As evident from eq. 2.9 at a given temperature electrons will predominate at sufficiently reducing conditions. A double-logarithmic plot of the electron concentration as a function of p_{O_2} will give a straight line with slope $-\frac{1}{6}$ [19]. However as we show in manuscripts II and III the conductivity of the disordered fluorites under investigation is virtually p_{O_2} independent, suggesting that electrons never predominate concentration wise and ions comprise the majority of charge carriers. Thus, the systems under consideration are regarded as ionic conductors.

Conferring to eq. 2.8 one can argue that tailoring of the ionic conductivity of a system can be achieved or by increasing the concentration of a charge carrier or increasing its mobility or both. I shall now discuss in the following section the mobility and concentration aspects.

Mobility

The charge mobility[8] of ionic defects i, u_i, relates to the ionic *random-diffusion* coefficient, D_i, through the Nernst-Einstein relation [19]:

$$D_i = u_i \frac{kT}{z_i e} \tag{2.11}$$

Moreover the random-diffusion coefficient of defect i, within the lattice from one site to another equivalent unoccupied site, can be related with the jump frequency of defect i, Γ_i:

$$D_i = \gamma \Gamma_i \lambda_i^2 \tag{2.12}$$

where λ_i denotes the effective defect i jump distance, and γ denotes a geometrical factor. The jump frequency is given by the number of jumps n, per time given by:

[8] Main assumption of the treatment in this paragraph is that the concentration of ionic defects is in equilibrium and not limited by kinetic effects, and that the defects do not interact with each other (unassociated)

$$\Gamma_i = \nu_0 \exp\left(-\frac{\Delta G_i^m}{kT}\right) \quad (2.13)$$

where ν_0 is the attempt frequency, ΔG_m, is the free energy of migration:

$$\Delta G_i^m = \Delta H_i^m - T\Delta S_i^m \quad (2.14)$$

ΔH_i^m is the migration enthalpy and ΔS_i^m is the entropy of migration. Combining eq. 2.11 to 2.14 the mobility of defect i reads:

$$u_i = u_{0,i}\ \frac{1}{T} \exp\left(-\frac{\Delta H_i^m}{kT}\right) \quad (2.15)$$

evidently the ΔH_i^m in eq. 2.15 dominates the temperature dependence of the ionic mobility. In eq. 2.15, $u_{0,i}$ is the pre-exponential term of mobility which relates to the attempt frequency, and/or the migration path of the respective species, given by:

$$u_{0,i} = \frac{z_i e}{k} \gamma \lambda_i^2 \nu_0 \exp\left(\frac{\Delta S_i^m}{k}\right) \quad (2.16)$$

Conventionally these factors, ν_0 and λ_i, are not expected to alter substantially from oxide to oxide. Yet, different species may behave differently in different oxides. In manuscript II we experimentally show that for the disordered fluorite $La_2Ce_2O_7$, the pre-exponential factor for protons is much lower than the one for oxide ions.

Concentration

In thermodynamic equilibrium the concentration of ionic defects c_i, is given by:

$$c_i = \widetilde{N}_i \exp(-\frac{\Delta G_i^{\mathrm{f}}}{kT}) = \widetilde{N}_i \exp\left(\frac{\Delta S_i^{\mathrm{f}}}{k}\right) \exp\left(-\frac{\Delta H_i^{\mathrm{f}}}{kT}\right) \quad (2.17)$$

where $\widetilde{N}_i$ is the product of concentration of sites times the number of configurations per site the defect may attain. ΔH_i^{f} and ΔS_i^{f}, are the enthalpy and entropy, respectively, associated with the introduction of one such defect into the lattice. The formalism and the thermodynamic considerations for the calculation of the defect formation energies are covered in subchapter 2.3.

Activation energy

Conferring to eq.2.8 and utilizing the equations for mobility (2.15 and 2.16) and concentration of ionic defects (eq.2.17) the Arrhenius type expression for the partial conductivity of ionic defect i reads:

$$\sigma_i T = \widetilde{N}_i \frac{z_i^2 e^2}{k} \hat{\gamma} a_0^2 \nu_0 \exp\left(\frac{\Delta S_i^m + \Delta S_i^f}{k}\right) \exp\left(-\frac{\Delta H_i^m + \Delta H_i^f}{kT}\right) = \sigma_{0,i} \exp\left(-\frac{E^a}{kT}\right) \quad (2.18)$$

where $\sigma_{0,i}$ is the pre-exponential term relating the mobility pre-exponential factors with the defect concentration, E^a is the activation energy for the conductivity. The derivation of eq.2.18 highlights that both the formation enthalpy of the defects and the energetic barrier that the defect has to overcome in order to migrate from one site to another contribute to the activation energy of the conductivity of a given material. Hence, both thermodynamic terms have to be favorable in order for the conductivity to be high.

Trapping

The main assumption of the treatment so far has been that the defects do not interact with each other, and, hence are randomly distributed. Yet, this is an idealized situation, and deviation from ideality has been found in many oxides. The intended formation of mobile charge defects by acceptor doping, may lead to electrostatic attraction between the acceptors and the mobile defects, what is commonly termed as *trapping*. Consequently, a mobile defect will have to overcome an energetic barrier to dissociate from this local bound state and enter the conductive state. As a result the activation energy of the defect in consideration may read:

$$E^a = \Delta H_i^m + \Delta H_i^f + \Delta H_i^t \quad (2.19)$$

where ΔH_i^t is the "extra" energetic barrier normally termed as *dissociation* enthalpy. Hence an oxide that experiences trapping this will exhibit a decrease in σ_i stemming from an increase in E^a. In manuscript III, we rationalize that the Ca acceptors induce a negative effect on the conductivity of the studied disordered fluorites and pyrochlores that is attributed to trapping of the charge carriers by the acceptors.

All in all the transport properties of mobile defects depend on their concentration, their ability to overcome the necessary energetic barrier in order to migrate from one site to another, and the migration path.

2.3 Computational methodology

"It is evidently equally foolish to accept probable reasoning from a mathematician and to demand from a rhetorician demonstrative proofs"

Aristotle

Nicomachean Ethics, 356 B.C

I shall now attempt to provide complementary material, from the *experimentalist's* point of view, on the basics and formalism of the computations we used based on density functional theory in manuscript I. We performed calculations to elucidate trends in the stability and electronic properties of defects and in hydration thermodynamics of pyrochlore oxides.

Density functional theory (DFT) is a quantum-mechanical approach for the computation of the electronic structure of matter. The central focus of DFT is the electron density, ρ, and the "functional" part of the term comes from the fact that the energy of the molecule is a function of the electron density, written $E[\rho]$, and the electron density is it self a function of position, $\rho(\mathbf{r})$ [2], thus one can write $E[\rho(\mathbf{r})]$. In mathematics a function of a function is called a functional.

2.3.1 Density functional theory formalism

The microscopic description of the physicochemical properties of matter can be expressed via a collection of coulombic (electrostatic) interactions of nuclei and electrons. In

principle all these properties can be derived from the quantum-mechanical wave function, Ψ, of the system under question:

$$(\mathbf{r}_1, \mathbf{r}_2, \ldots, \mathbf{R}_1, \mathbf{R}_2, \ldots; t) \qquad (2.20)$$

where $\mathbf{r}_i$ and $\mathbf{R}_i$ denote the coordinates of the electrons and nuclei in the system respectively. The time-independent Schrödinger equation written in the succinct form:

$$\widehat{H}\,\Psi = \mathrm{E}\Psi \qquad (2.21)$$

may, in principle, assist to determine the wave function, where E is the energy of the system. The term $\widehat{H}$ is the Hamiltonian operator given by:

$$\widehat{H} = \sum_{i=1}^{N} -\frac{1}{2}\nabla_i^2 + \sum_{i}^{N} w(\mathbf{r}_i) + \frac{1}{2}\sum_{i\neq j}^{N} \frac{1}{(\mathbf{r}_i - \mathbf{r}_j)} \qquad (2.22)$$

and corresponds to the total energy of the system, *i.e.* the sum of the kinetic and potential energy of all the N electrons of the system. However, solving the Schrödinger equation is far beyond today's computational capabilities. Hence, one must involve some approximations to circumvent this challenge. DFT is a method that we can use to obtain an approximate solution to the Schrödinger equation.

2.3.2 Approximations

In order to simplify many-atom problems we can reduce the degrees of freedom by separating them into nuclear and electronic. A way to do so is by assuming that a nucleus is held fixed in position during the period of an electron's motion, since an electron moves faster than a nucleus. This assumption in known as the Born-Oppenheimer approximation [25], and a many-atom problem breaks down to an electronic and a nuclear problem. In that manner the electronic problem is solved for a fixed nuclear configuration giving rise to an external potential, $\widehat{V_{\mathrm{ext}}}$, from the interaction of the electron with the atomic nuclei. Then the Hamiltonian for the electronic system may be given by:

$$\widehat{H} = \sum_{i=1}^{N} -\frac{1}{2}\nabla_i^2 + \widehat{V_{\mathrm{ext}}} + \frac{1}{2}\sum_{i\neq j}^{N} \frac{1}{(\mathbf{r}_i - \mathbf{r}_j)} \qquad (2.23)$$

Yet, the electron-electron interaction expressed in the third term of eq. 2.23 is rather complicated and demanding to treat, and we still have to deal with a wave function of $3N$ variables.

If we instead use the electron density, which is a function of space and time we go from a $3N$-dimensional problem to an *only* 3-dimensional problem. Hohenberg and Kohn in [26], formulated a theorem in two parts regarding the ground-state electronic density. The first part shows that the external potential $\widehat{V_{\text{ext}}}$ of an electronic system is determined by the ground-state electronic density $\rho_0(\text{r})$. Given that the Hamiltonian operator is specified by the external potential, then the electron density uniquely determines the Hamiltonian operator of eq. 2.23. The second part of the theorem formulates the relationship between the ground-state energy and the electron density.

Kohn and Sham [27] introduced a fictitious system of non-interacting electrons and isolated the many-atom effects of a real system into one unknown energy term. The electron density functional may be expressed:

$$\text{E}[\rho(\mathbf{r})] = E_K + E_{P;e-\text{n}} + E_{P;e-e} + E_{\text{xc}}[\rho] \quad (2.25)$$

where E_K is the total kinetic energy, $E_{P;e-\text{n}}$ is the electron-nucleus potential energy, $E_{P;e-e}$ is the electron-electron potential energy, and $E_{\text{xc}}[\rho]$ is the exchange correlation energy, which takes into account all the many-atom effects. The two difficult terms to calculate here are the E_K and $E_{\text{xc}}[\rho]$. Applying the variation principle in order to minimize the $\text{E}[\rho(\mathbf{r})]$ will lead us to the Kohn-Sham equations:

$$\left\{-\frac{1}{2}\nabla^2 + V(\mathbf{r})\right\}\psi_i(\mathbf{r}) = \varepsilon_i\psi_i(\mathbf{r}) \quad (2.26)$$

The term $V(\mathbf{r})$ contains the electron-nucleus attraction, the electron-electron repulsion, and the very important exchange-correlation potential V_{xc}, which is the functional derivative of the exchange-correlation energy:

$$V_{\text{xc}}[\rho] = \frac{\delta E_{\text{xc}}[\rho]}{\delta\rho} \quad (2.27)$$

Eq.2.27 is solved iteratively, given an initial guess of $E_{\text{xc}}[\rho]$, until a self consistent solution is found. The first approximation of the $E_{\text{xc}}[\rho]$ is the so called local-density approximation (LDA) as proposed by Kohn and Sham [27]:

$$E_{\mathrm{xc}}[\rho] = \int \rho(\mathbf{r})\varepsilon_{\mathrm{xc}}[\rho(\mathbf{r})]d\mathbf{r} \qquad (2.28)$$

where $\varepsilon_{\mathrm{xc}}$ is the exchange-correlation energy per electron in a homogenous gas of constant density. However electron density is rarely homogenous, therefore a more sophisticated approximation is used, the generalized gradient approximation (GGA). In GGA the $\varepsilon_{\mathrm{xc}}$ is considered a function of the local density and its gradient.

Using empirical fitting of parameters based on experimental results and combining theoretical methods functionals may be constructed, in practice the choice of which $\varepsilon_{\mathrm{xc}}$ to use breaks down to testing and knowledge gained from experimental work.

2.3.3 Point defect calculations

The formalism for the calculation of a point defect in a system is based on the energy difference before and after the formation of the defect, taking into account the chemical potential of the reference states, with which atoms are exchanged. Chemical potentials can be thought of as the energy cost of exchanging atoms with a reservoir of such atoms. Correspondingly, when defect formation involves removing an atom from the material the energy after formation will have a contribution from the chemical potential of the removed atom in its corresponding reservoir [28]. In that manner we may formulate the energy for defect formation as:

$$\Delta G^{\mathrm{f}}_{\mathrm{Defect}} = E^{\mathrm{tot}}_{\mathrm{Defect}} - E^{\mathrm{tot}}_{\mathrm{Bulk}} + \sum_{i=1}^{N} n_i\mu_i + q\mu_e \qquad (2.29)$$

where $E^{\mathrm{tot}}_{\mathrm{Bulk}}$ is the total energy of the pristine lattice before defect formation and $E^{\mathrm{tot}}_{\mathrm{Defect}}$ is the total energy of the defective lattice after defect formation, n_i is the number of atoms exchanged, upon defect formation with chemical potentials μ_i. The last term $q\mu_e$ contains the energy related to electronic exchange upon defect formation, where q is the effective charge of the defect and μ_e is the electronic chemical potential.

Moreover, the $q\mu_e$ term in equation 2.29 measures the energetic cost associated with the exchange of q electrons between the defect and the electrochemical environment. In a situation prior to the formation of any defects the μ_e will be pinned to the center of the

band gap. However in the presence of defects the value of μ_e will depend on the concentration and the electronic properties of the defects. In order to avoid possible implications, we introduce an electrostatic term, $\Delta\epsilon$ that aligns the core levels of the defective and pristine cell, and eq. 4.10 may be re-written

$$\Delta G^{\mathrm{f}}_{\mathrm{Defect}} = E^{\mathrm{tot}}_{\mathrm{Defect}} - E^{\mathrm{tot}}_{\mathrm{Bulk}} + \sum_{i=1}^{N} n_i\mu_i + q(\varepsilon_{\mathrm{f}} + \Delta\epsilon) \qquad (2.30)$$

where ε_{f} is the Fermi level of the pristine cell.

As we discussed in the proceeding chapter, the stability of protonic defects and oxygen vacancies in the studied systems, is strongly dependent on the temperature and the atmosphere. In order to calculate point defect formation energies for finite temperature and partial pressure, the dependencies of partial pressure and temperature on atomic chemical potentials should be included:

$$\mu_i = \mu_i^{\circ} + \mu_i(T, p^{\circ}) + kT\ln\left(\frac{p_i}{p^{\circ}}\right) \qquad (2.31)$$

where μ_i° are set to the total energies of the pristine phase while $\mu_i(T, p^{\circ})$are the tabulated temperature dependencies of the atomic chemical potentials [29]. Finally combining equations 2.29 and 2.30 the defect concentration per site for a finite temperature and pressure will be given:

$$\frac{c_i}{[\mathrm{site}]} = N_{\mathrm{config}} \exp\left(-\frac{\Delta G^{\mathrm{f}}_{\mathrm{Defect}}}{kT}\right) \qquad (2.32)$$

where [site] is the concentration of sites on which the defect may form and N_{config} is the number of configurations per site that the defect may attain. Substituting the product $\widetilde{N}_i = [\mathrm{site}] \cdot N_{\mathrm{config}}$ we obtain eq. 2.17.

3. Phenomenological aspects and concepts of electrodics

Moving away from the study of ionic transport and defects in disordered fluorites that may consist the electrolyte in a PC-SOFC, we now come to the electrochemical phenomena that occur at the interface between the fluorite electrolyte and the electrode. Electrodes in a PC-SOFC provide or remove both electric charge (ions and electrons) and mass, *i.e.* fuel oxidant, and water. For example, the introduction of protons from the fuel *i.e.* H_2, into the electrolyte can be achieved by using porous Pt electrodes applied onto the electrolyte. In this case the process takes place at the interface between the electrode, the electrolyte, and the fuel, the so-called triple phase boundary (TPB). In this chapter I introduce the basic concepts on electrodes, and the utilized phenomenology for their study.

3.1 Cathode

Under operating conditions in a PC-SOFC, protons depart from the electrolyte and arrive to the cathode where they undergo the following reaction:

$$2H^+ + 2e^- + \frac{1}{2}O_2(g) \rightarrow H_2O(g) \qquad (3.1)$$

The flow of charge carriers consumed in this reaction delivers some portion to the overall reversible work converted to electrical work. The amount of electrical work produced depends on the internal losses in the cell, including overpotential losses at the cathode. One of the first studies on polarization phenomena on PC-SOFCs by Uchida *et al.* [30] using Pt, as electrodes showed that the polarization of the cathode could not be neglected below 900 $^{\circ}$C.

Oxygen gas that reaches the cathode diffuses into the open pores and is reduced somewhere within the electrode matrix reacting with the protons arriving from the electrolyte. Evidently the cathode should meet manifold complex requirements, namely, adequate porosity - for gas diffusion, high electronic and ionic conductivity - for current distribution, superior catalytic activity - for oxygen reduction, chemical and thermal compatibility with the electrolyte, and long-time performance.

Despite the very good catalytic activity of noble metals such as Pt, their high cost makes them a not feasible choice towards the commercialization of PC-SOFCs. Moreover, the same study by Uchida *et al*.[30] suggested surface diffusion of adsorbed oxygen atoms to the electrochemically active site on the electrolyte, as the rate determining step for the cathodic reaction. The latter may suggest that purely electronically conducting electrodes are insufficient, and electrode materials permeable to oxygen via ambipolar transport of oxide ions or via atomic transport might be more suitable. Yet, a main concern is the reaction between oxide ions and protons arriving from the electrolyte to form water at the electrode / electrolyte interface which can lead to electrode degradation. Hence, the incorporation of a protonic phase into the electrode can facilitate the proton diffusion within the cathode bulk, and water formation will not anymore be limited within the electrode / electrolyte interface. Moreover, the incorporation of the protonic phase enhances the active area of the electrochemical reaction. For that purpose the use of mixed ionic (protons and oxide ions) electronic conducting (MIEC) cathodes has been much studied (suggestively: [7, 31-36]).

Nevertheless, for a systematic and targeted electrode development, a deeper understanding of the underlying transport and reaction mechanisms and the correlation to materials properties is required. Keeping this in mind for the development of fuel cells based on $La_{5.6}WO_{11.4}$, in manuscript IV we attempted to rationalize the rate determining step of the cathode reaction for the studied systems.

3.1.1 Possible mechanisms and rate limiting steps

In manuscript IV we divided the cathode reactions with respect to the distribution of relaxation times and atmosphere dependencies, into two categories. The first category concerns reactions occurring on the surface of the electrode, involving exchange and diffusion of adsorbed species and red-ox reactions. The second category involves charge

transfer reactions across the cathode/electrolyte interface. All of these processes require a driving force and thus they all potentially contribute to the overpotential.

Uchida *et al.*[30] proposed the elementary reaction steps for a PC-SOFC cathode, using Pt as a model electrode, investigating the pO_2 dependence of the cathode polarization resistance. He *et al.* [37] investigated the polarization resistance of $Sm_{0.5}Sr_{0.5}CoO_{3-\delta}$–$BaCe_{0.8}Sm_{0.2}O_{3-\delta}$ composite cathode on $BaCe_{0.8}Sm_{0.2}O_{3-\delta}$ electrolyte as a function of pO_2 and pH_2O to determine rate limiting steps. They proposed a cathode reaction model consisting of eight elementary steps and calculated the reaction order of each step. From the reaction order and the dependency of the polarization resistance on pO_2 and pH_2O they were able to elucidate the rate limiting step for the oxygen reaction on the cathode under study. Yet, it should be mentioned that the reaction rates in the proposed model cannot serve as a panacea in all cases, given the complexity of the studied systems, and the plethora of charge carriers. In manuscript IV, in order to identify the rate determining steps of the oxygen reduction at the studied cathode we examined the dependence of the polarization resistance on pO_2 and pH_2O.

3.2 Anode

The electrochemistry on the anode side is seemingly simpler compared to the cathode, as it involves *only* the oxidation of the fuel, and it is worth to mention that electrochemical and morphological characterization of anode for PC-SOFCs has not received much attention in literature. However as stated earlier for the cathode, in order for the anode to perform, it has to meet various requirements, for the most part the same as for the cathode. The anode should reveal high electrocatalytic activity towards fuel. The latter has been the main reason for the use of Ni or Ni cermets, when hydrogen is the fuel, as Ni reveals high electrocatalytic activity towards hydrogen. Yamaguchi *et al.* [38] studied the performance of hydrogen permeable metal anodes as Pd, Pd-Ag, and a porous Ni anode, based on voltage losses. For the porous Ni anode the overall reaction when using hydrogen as a fuel is:

$$H_2(g) \rightarrow 2H^+ + 2e^- \tag{3.2}$$

While in the case of the hydrogen permeable metal anodes, where hydrogen exists in the atomic form, the expected reaction reads:

$$H \rightarrow H^+ + e^- \quad (3.3)$$

Based on reaction 3.3 Yamaguchi *et al.* claimed that in the hydrogen permeable anodes of their study, the fuel oxidation proceeds faster than in porous Ni, as the dissociation process of hydrogen is not contained in the reaction. However, research on anodes for PC-SOFC is mainly focused towards Ni and Ni cermets due to the higher price of Pd and Ag compared to Ni.

3.3 Phenomenology

Given the similarity of the nature of the electrochemical processes occurring at the anode and the cathode in the subsequent part I will use the cathode as reference point.

The polarization area specific resistance, R_p $(\Omega \cdot \mathrm{cm}^2)$, is an important phenomenological measure of the potential drop, when evaluating the performance of the cathode. As a phenomenological parameter, R_p has different constituents rising from the interplay between materials property and microstructural processing. For instance, in a PC-SOFC the R_p of the cathode is related to the reaction 3.1. A convenient way to treat R_p is to express it as the sum of the individual resistances, R_i, associated with one elementary reaction step i. In that manner R_p reads:

$$R_\mathrm{p} = \sum_{i=m}^{n} R_i \times A \quad (3.4)$$

where A is the area of the cathode. From the discussion in the preceding paragraphs it is clear that the polarization resistance contains terms that may be associated with microstructural processing, for instance gas diffusion, grain size, TPB length, and cathode effective area, rather than materials properties. Parameters such as activation energy, E_a, and pressure dependencies need to be determined in order to precisely describe the overall performance of the electrode.

There is a direct connection between the behaviour of a physical system, like the systems studied in this thesis, and an idealized model circuit consisting of discrete electrical components. This connection exists through the fundamental laws which connect charge

and potential. Electrochemical impedance spectroscopy (EIS) is a technique that may be used in order to utilize this connection for the interpretation of the measured data.

Through our studies we fitted the impedance spectra to equivalent circuits which are representative of the electrochemical processes taking place in the systems under investigation, with respect to the distribution of relaxation times of each process. However circuit elements are based on fundamental principles and can be considered as *ideal* transfer functions. A recurring phenomenological dispersion function is the constant phase element (CPE) [39], presented in the admittance plane by:

$$Y_{\mathrm{CPE}} = Y(j\omega)^n = Y_0\omega^n\cos\left(\frac{n\pi}{2}\right) + jY_0\omega^n\sin\left(\frac{n\pi}{2}\right) \quad (3.6)$$

where $j = \sqrt{-1}$, and ω is the angular frequency. The parallel combination of a CPE and a resistor presents a depressed semicircle in the impedance plane cf. Fig. 3.1. The CPE is a generic transfer function, and for $n = 1$ it represents a capacitor (C), for $n = 0.5$ a Warburg element (W), for $n = 0$ a resistor (R), and for $n = -1$ an inductor (L). The frequency of the apex corresponds to the characteristic frequency ω_0 of the circuit given by:

$$\omega_0 = \frac{1}{2\pi\mathrm{RC}} \quad (3.7)$$

The quasi-equivalent capacitance C of the CPE may be calculated from:

$$\mathrm{C}=Y^{\frac{1}{n}}R^{\left(\frac{1}{n}-1\right)} \quad (3.8)$$

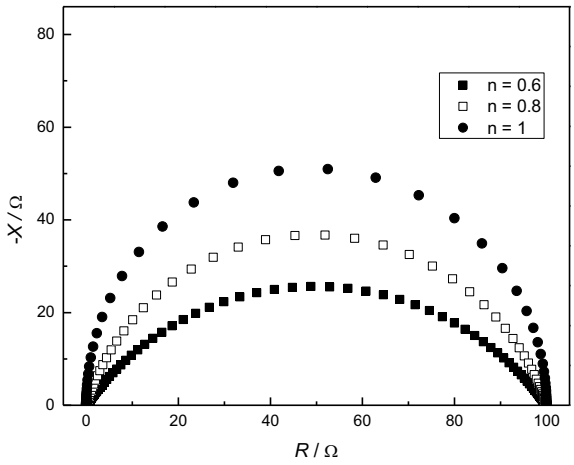

Figure 3.1 Impedance spectra in Nyquist representation of a parallel circuit of a resistor and a CPE.

In semi-conductors and in many poly-crystalline oxides, in particular, electrical circuits consisting of series of parallel combinations of a resistor and a capacitance or a CPE are often utilized to analyse electrical and electrochemical properties of grains, grain boundaries and electrodes. However, electrodes are commonly described by Randles-type[9] circuits as the one shown in Fig. 3.2.

Electrodes are in contact with the electrolyte. The interface between the electrode and the electrolyte is assigned to a capacitance and denoted as the double-layer capacitance, C_{dl}. Unlike grain boundaries, we have only one or two electrodes, so the C_{dl} becomes big, typically in the order of $\mu F \cdot cm^{-2}$. Moreover, electrodes have a charge transfer resistance R_{CT} in parallel with C_{dl}. In practise R_{CT} can represent both the path electrons and ions use to jump activation barriers, and the processes at the electrode / electrolyte interface where electrons and chemical species are involved.

Several transport processes take place in series during charge transfer at the electrode *i.e.* gas diffusion and diffusion of species, and adsorption-desorption. These processes are attributed to chemical storage of species and give rise to high capacitances, in the order of

[9] For the analysis of interfacial electrochemical reactions in presence of semi-infinite linear diffusion of electroactive species to electrodes, the proposed equivalent circuit by Randles consists of a Warburg element instead of the Q_D and R_D in parallel [40] J.E.B. Randles, *Discussions of the Faraday Society* **1** (1947) (0) 11.

$mF \cdot cm^{-2}$. The resistance of this processes may be large or small. For simplicity we may refer to this element as diffusion resistance R_D. In the Randles-type circuit this process is represented by the constant phase element, Q_D, and R_D in parallel. If the diffusion resistance is infinitely large, the parallel Q_D, and R_D reduces to Q_D, cf. Fig 3.2.

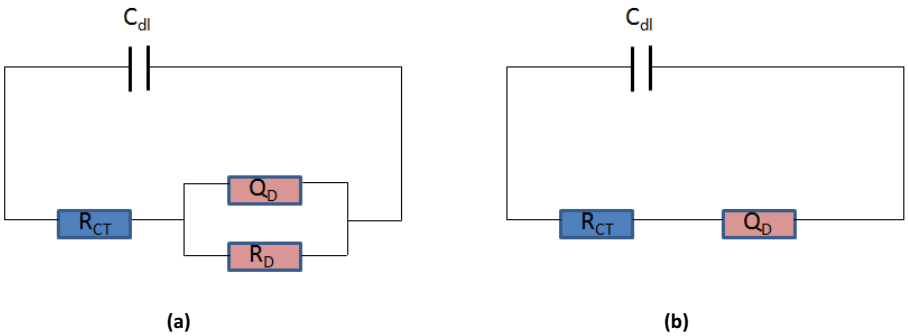

Figure 3.2 Schematic diagram of a Randles-type circuit.

4. **Manuscripts**

Manuscript I	Hydration thermodynamics of pyrochlore structured oxides from TG and first principles calculations *Dalton Transactions*, **41(43)**, 13343-13351, (2012) T.S Bjørheim, V. Besikiotis, R. Haugsrud
Manuscript II	Crystal structure hydration and ionic conductivity of the inherently oxygen-deficient $La_2Ce_2O_7$ *Solid State Ionics*, **228**,1-7 (2012) V. Besikiotis, C. S. Knee, I. Ahmed, R. Haugsrud, T. Norby
Manuscript III	Conductivity and hydration trends in disordered fluorite and pyrochlore oxides: A study on lanthanum cerate-zirconate based compounds *Solid State Ionics*, **229**, 26-32 (2012) V. Besikiotis, S. Ricote, M.H. Jensen, T. Norby, R. Haugsrud
Manuscript IV	On La_2NiO_4 as cathode on lanthanum tungstate $La_{5.6}WO_{11.4}$ electrolyte *To be submitted* V. Besikiotis, R. Strandbakke, T. Norby

Manuscript I:

Hydration thermodynamics of pyrochlore structured oxides from TG and first principles calculations

Dalton Transactions, **41(43)**, 13343-13351, (2012)

T.S Bjørheim, V. Besikiotis, R. Haugsrud

Erratum

The correct form of eq. 11 is:

$$[\mathrm{OH}_{\mathrm{O}}^{\bullet}] = \frac{K_{\mathrm{hydr}}\left(N_{\mathrm{s,OH}_{\mathrm{O}}^{\bullet}} N_{\mathrm{c,OH}_{\mathrm{O}}^{\bullet}}\right)^2}{4 N_{\mathrm{s,v}_{\mathrm{O}}^{\bullet\bullet}} N_{\mathrm{c,v}_{\mathrm{O}}^{\bullet\bullet}}} \left(\frac{p_{\mathrm{H_2O}}}{p^{\circ}}\right) \left(-1 + \sqrt{1 + \frac{8 N_{\mathrm{s,v}_{\mathrm{O}}^{\bullet\bullet}} N_{\mathrm{c,v}_{\mathrm{O}}^{\bullet\bullet}} [\mathrm{Ca}_{\mathrm{RE}}^{\prime}]}{K_{\mathrm{hydr}}\left(N_{\mathrm{s,OH}_{\mathrm{O}}^{\bullet}} N_{\mathrm{c,OH}_{\mathrm{O}}^{\bullet}}\right)^2 \left(\frac{p_{\mathrm{H_2O}}}{p^{\circ}}\right)}} \right)$$

Dalton Transactions

Dynamic Article Links

Cite this: *Dalton Trans.*, 2012, **41**, 13343

www.rsc.org/dalton

PAPER

Hydration thermodynamics of pyrochlore structured oxides from TG and first principles calculations

Tor S. Bjørheim, Vasileios Besikiotis and Reidar Haugsrud*

Received 10th July 2012, Accepted 24th August 2012
DOI: 10.1039/c2dt31517c

In this contribution we investigate trends in the defect chemistry and hydration thermodynamics of rare-earth pyrochlore structured oxides, $RE_2X_2O_7$ (RE = La–Lu and X = Ti, Sn, Zr and Ce). First principles density functional theory (DFT) calculations have been performed to elucidate trends in the general defect chemistry and hydration enthalpy for the above-mentioned series. Further, to justify the use of such theoretical methods, the hydration properties of selected compositions were studied by means of thermogravimetric measurements. Both DFT calculations and TG measurements indicate that the hydration enthalpy becomes less exothermic with decreasing radii of RE ions within the $RE_2X_2O_7$ series (X = Ti, Sn, Zr and Ce), while it is less dependent on the X site ion. The observed hydration trends are discussed in connection with trends in the stability of both protons and oxygen vacancies and changes in the electronic density of states and bonding environment through the series. Finally, the findings are discussed with respect to existing correlations for other binary and ternary oxides.

1 Introduction

Oxide ceramics display numerous functional properties which are widely utilised in applications covering a range of fields from low temperature photocatalytic applications to high temperature solid oxide fuel cells. Hydrogen, being omnipresent as $H_2(g)$ or $H_2O(g)$, is often found as a dominating defect in the form of substitutional hydroxide defects ($OH_O^{\bullet}$) in oxides. Hydration of oxygen vacancies ($v_O^{\bullet\bullet}$) is the most commonly parameterised equilibrium for incorporation of these protonic defects

$$H_2O(g) + v_O^{\bullet\bullet} + O_O{}^X = 2OH_O^{\bullet} \quad (1)$$

with an equilibrium constant given by

$$K_{hydr} = \exp\left(\frac{\Delta_{hydr}S^o}{R}\right)\exp\left(-\frac{\Delta_{hydr}H^o}{RT}\right) \quad (2)$$

where $\Delta_{hydr}S^o$ and $\Delta_{hydr}H^o$ are the standard hydration entropy and enthalpy, respectively. The hydration entropy typically is reported to attain values of -120 ± 40 J mol^{-1} K^{-1} with no apparent compositional dependence.[1] The hydration enthalpy, on the other hand, is materials dependent, and found to range from around -220 kJ mol^{-1} for Y_2O_3 and Er_2O_3,[2] to positive values in ZrO_2 or CeO_2.[1] While the two former oxides remain hydrated to above 1000 °C in wet atmospheres, hydration is insignificant in the two latter.

Over the last few decades it has been shown that many ceramic oxides display significant proton conduction, even at temperatures up to 1000 °C. The most commonly studied oxides are those crystallising in the perovskite structure (ABO_3) where systems such as acceptor doped $BaZrO_3$, $BaCeO_3$ and $SrCeO_3$ display proton conductivities in the order of 10^{-2} S cm^{-1} at 800 °C[3–6] in wet atmospheres. However, the applicability of these oxides is limited by high grain boundary resistance and instability towards $CO_2(g)$, and at moderate temperatures also towards $H_2O(g)$. Although various non-Ba containing oxides, for instance within the monazite ($LaPO_4$,[7] $LaVO_4$[8] and $LaAsO_4$[9]) and scheelite ($LaNbO_4$) families,[10,11] and in the rare-earth pyrochlore family of oxides, $RE_2X_2O_7$ (X = Ti, Sn, Zr and Ce),[12–18] display proton conduction, the partial proton conductivity is generally significantly lower than those of the state-of-the-art perovskites. Acceptor doped $La_2Zr_2O_7$ is the most widely studied rare-earth based pyrochlore oxide in terms of proton conduction[12–15] and displays a maximum proton conductivity of 10^{-3} S cm^{-1}.

In the search for materials with high proton conductivity, a more fundamental understanding of possible correlations between hydration and proton transport in the oxides and other fundamental properties such as elemental composition and structure has been sought during the last two decades. The hydration reaction (eqn (1)) may be viewed as a two-step process in which an oxygen vacancy first is filled by an oxide ion, followed by protonation of two lattice oxide ions

$$v_O^{\bullet\bullet} + 2e^{/} + \tfrac{1}{2}O_2(g) = O_O^X \quad (3)$$

$$H_2O(g) + 2O_O^X = 2OH_O^{\bullet} + 2e^{/} + \tfrac{1}{2}O_2(g) \quad (4)$$

Both processes may be regarded as Lewis acid/base reactions, and an oxide's hydration properties are often linked to its basicity through the electronegativity of the cations (for instance in

Department of Chemistry, University of Oslo, FERMiO, Gaustadallèen 21, NO-0349 Oslo, Norway. E-mail: reidarha@kjemi.uio.no

the case of perovskites[5,6]). In other oxide series, such as the rare-earth sesquioxides and niobates, it seemingly to a large extent is the size of the cations which determines the hydration properties.[2,10] These two rather different empirical correlations reflect the intricate nature of the hydration thermodynamics of oxides, which we will elaborate on in the following section.

2 Hydration trends of binary and ternary oxides

For the perovskite series $Ba(Zr_{1-x}Y_x)O_3$, $Ba(Ce_{1-x}Y_x)O_{3-\delta}$ and $1/2Ba_2(Sn_{2-x}Y_x)O_{5.5-\delta}$, Kreuer[3,5] reported an increasingly exothermic hydration enthalpy with increasing Y content, which was attributed to increasing basicity of the oxide ions. This observation has later been supported by computational charge density analyses on Y doped $BaCeO_3$,[19] showing increasing charge of the oxygen ions with increasing Y content. Norby *et al.*[1] proposed a more general correlation relating hydration of oxygen vacancies to the difference between the electronegativity of the B and A site cations within the perovskite series; the smaller the difference, the more exothermic the hydration enthalpy is. It has later been argued that the correlation also holds for both systems in which B is more electronegative than A, and *vice versa*.[20] The hydration enthalpy has also been related to Goldschmidt's tolerance factor of the perovskites; the lower the tolerance factor, the more exothermic is the hydration enthalpy.[20]

In the case of the rare-earth sesquioxides, RE_2O_3, Norby and Larring[2,21] showed that the enthalpy of hydration according to eqn (1) becomes more exothermic with decreasing size of the RE ion (and thus increasing stability of the oxides), attributed to decreasing stability of oxygen vacancies.

For the scheelite structured rare-earth ortho-niobates, $RENbO_4$, Haugsrud and Norby[10] also showed that the hydration enthalpies become more exothermic with decreasing size of the RE ion. Further, for the structurally similar monazites, $LaXO_4$ (X = P, As and V), only a minor dependence of the hydration enthalpy on the X site element was encountered,[8,9] thus showing that the two cations do not affect the hydration enthalpy in a 'simple' manner, such as for the perovskites.

For pyrochlore structured oxides, trends in the hydration thermodynamics are more unclear. Knee *et al.*[18] investigated the $Sm_2X_2O_7$ series (X = Ti, Sn, Zr and Ce) and found that the hydration thermodynamics were dependent on the X site element, with the smaller cations displaying the highest levels of hydration. Furthermore, $Sm_2Ti_2O_7$ [18] exhibits higher proton conductivity than $Er_2Ti_2O_7$ which only displays a minor contribution from protons to the bulk conductivity at the lowest temperatures ($T < 350$ °C).[22] Eurenius *et al.*[17] also reported the water uptake in the $RE_2Sn_2O_7$ (RE = La, Sm and Yb) to decrease with decreasing RE size. This suggests that the hydration enthalpy increases (less exothermic) with decreasing size of the RE ion, *i.e.* opposite to the rare-earth sesquioxides and niobates. In this respect, it is interesting to note that the trends in formation enthalpy for the pyrochlore[23] and monazite $REXO_4$ (X = P and V)[24] series of compounds concur; the formation enthalpy increases (less stable oxides) with decreasing RE size, while it is opposite for the rare earth sesquioxides. Furthermore, within the pyrochlore series, the deviation from the ideal pyrochlore structure has been related to the r_{RE}/r_X ratio, and the degree of anion and cation disorder increases when the ratio decreases.[25,26] In this respect, Besikiotis *et al.*[27] recently showed that the hydration enthalpies of the two end-members in the series $La_2(Ce_xZr_{1-x})_2O_7$ ($x = 0$ and $x = 1$) were similar, whereas those of the substituted compositions were less exothermic. The behaviour was attributed to the gradual ordering of the cation and anion lattice with increasing Zr content.

As trends in the hydration enthalpies most likely are dependent on structural changes through a series of oxides, we have in this work focused on pyrochlore structured oxides, which attain the cubic $Fd\bar{3}m$ structure for a large variety of compositions. We investigate the general defect chemistry and trends in the hydration thermodynamics through the $RE_2X_2O_7$ pyrochlore series by first principles density functional theory (DFT) calculations. The calculations are limited to selected compositions with the ordered pyrochlore structure, *i.e.* $RE_2X_2O_7$ with RE = La–Lu and X = Ti, Sn or Zr. For comparison, we also include selected rare-earth cerates, $RE_2Ce_2O_7$, although these experimentally take on disordered pyrochlore related structures.[28] The observed trends are, moreover, supplemented with thermogravimetric measurements (TG) of the water uptake in selected $RE_2Sn_2O_7$ compositions. The trends are discussed in relation to the bonding environment of protons and oxygen vacancies, charge density of the oxide ions, and changes in the electronic structure upon defect formation. Finally, the characteristics of these pyrochlores are discussed and compared with existing empirical trends for other series of oxides.

3 Experimental

$La_{1.8}Ca_{0.2}Sn_2O_{7-\delta}$, $Sm_{1.8}Ca_{0.2}Sn_2O_{7-\delta}$ and $Er_{1.8}Ca_{0.2}Sn_2O_{7-\delta}$ were prepared by the solid state reaction with La_2O_3 (99.9%), Sm_2O_3 (99.9%) and Er_2O_3 (99.9%) supplied by Alfa Aesar. All starting powders were dried at 950 °C for 1 h prior to weighing due to their hygroscopic nature. Stoichiometric amounts of the precursors were ball milled in isopropanol, calcined at 1000 °C for 10 h in air, and finally remixed in a mortar before a second calcination at 1350 °C for 10 h. Structural characterisation of the as-prepared powders was performed by X-ray diffraction (XRD), utilising a Siemens D5000 diffractometer with $CuK_{\alpha 1}$ radiation. All X-ray patterns could be refined in the pyrochlore ($Fd\bar{3}m$) structure, but also with minor amounts of $CaSnO_3$, indicating that the solubility of Ca in the series of $RE_2Sn_2O_7$ is rather limited.

The relative weight change as a function of temperature in wet air ($p_{H_2O} = 0.025$ atm) was studied by means of thermogravimetry (TG) using a Netzsch STA 449 F1 Jupiter. The measurements were performed isobarically as a function of temperature in the range from 1000 to 300 °C. The samples were allowed to equilibrate for 5 h at each temperature, with a cooling rate of 50 °C h^{-1} between the temperature steps.

4 Computational methodology

4.1 Computational details

The calculations in this work were performed within the density functional theory (DFT) formalism, using the VASP code.[29,30]

Exchange and correlation effects were described by the generalized gradient approximation functional due to Perdew, Burke and Ernzerhof (GGA-PBE)[31] and the projector augmented-wave (PAW) method for the electron–ion interactions.[32] A constant cut-off energy of 500 eV for the plane-waves was used in all calculations. Bader charge density analyses were performed on selected compositions according to ref. 33.

As the $Fd\bar{3}m$ unit cell of $RE_2X_2O_7$ encompasses 88 atoms with lattice constants of 10–11 Å, a single unit cell was used in all calculations. The pristine structures were optimised prior to the defect calculations by relaxing all lattice volumes, shapes and ionic positions until the residual forces were smaller than 0.02 eV $Å^{-1}$, with an energy convergence criterion of 10^{-6} eV for self-consistency. Defect calculations were performed with a single defect in each cell with the total charge adjusted to reflect the desired charge state of the defect.

Phonon calculations of the $OH_O^{\bullet}$ defect and bulk O atoms were performed using accurately optimised structures, for which the convergence criteria were decreased to 10^{-4} eV $Å^{-1}$ and 10^{-8} eV. The vibrational modes were calculated within the harmonic approximation from finite displacements. In the case of $OH_O^{\bullet}$, we allow displacements of the $OH_O^{\bullet}$ itself and the two nearest O atoms, while for bulk O we only displace the O atom. A finite displacement length of 0.015 Å in all directions was used for all calculations.

Rare-earth pyrochlores encompass RE and X cations coordinated to 8 and 6 O ions, respectively, two coordination-wise non-equivalent occupied oxygen sites, O48f and O8b, and an unoccupied interstitial site, v_{i8a}. The O48f sites are located in the XO_6 octahedron, and are thus coordinated to both the RE and X cations, while the O8b sites are coordinated only to the RE cations. Similarly, the unoccupied v_{i8a} sites are coordinated only to the X site cation. Hence, we have in this work considered defect formation at all oxygen sites, *i.e.* $v_{O8b}^{\bullet\bullet}$, $v_{O48f}^{\bullet\bullet}$, $OH_{O8b}^{\bullet}$, $OH_{O48f}^{\bullet}$, $O_{i8a}^{''}$ and $OH_{i8a}^{'}$.

4.2 Thermodynamic formalism

All defect formation energies were obtained through

$$\Delta G_{\text{defect}}^{\text{f}} = E_{\text{defect}}^{\text{tot}} - E_{\text{bulk}}^{\text{tot}} + \sum_{i=1}^{\text{N}} \Delta n_i \mu_i + q(\varepsilon_{\text{f}} + \Delta \in) \qquad (5)$$

where $E_{\text{defect}}^{\text{tot}}$ and $E_{\text{bulk}}^{\text{tot}}$ are the total energies of the defective and pristine supercells, respectively, Δn_i is the change in the number of atom i with chemical potentials μ_i upon defect formation. Further, q is the charge of the defect and ε_{f} is the Fermi level of the pristine cell. $\Delta\epsilon$ is an electrostatic term aligning the core levels of the pristine and defective supercells in order to account for the artificial interactions caused by the jellium background in the charged, defective systems.[34] Finite temperature and partial pressure formation energies were obtained by including the partial pressure dependencies and tabulated temperature dependencies on all atomic chemical potentials in eqn (5), according to

$$\mu_i = \mu_i^{\text{o}} + \mu_i(T, p^{\text{o}}) + k_{\text{b}} T \ln\left(\frac{p_i}{p^{\text{o}}}\right) \qquad (6)$$

where μ_i^{o} are set to the total energies of the pure phases as obtained through DFT, while $\mu_i(T,p^{\text{o}})$ are the tabulated temperature dependencies of the atomic chemical potentials.[35] This approach effectively neglects contributions from vibrational changes within the crystal itself upon defect formation. However, to estimate trends in the solid state vibrational contributions to the thermodynamics of the hydration reaction (eqn (1)), we have applied a simplified Boltzmann model where all vibrational modes are assumed to be purely harmonic and independent, with their free energies given by

$$G_j(T) = \frac{h\nu_j}{2} + k_{\text{b}} T \ln\left[1 - \exp\left(-\frac{h\nu_j}{k_{\text{b}} T}\right)\right] \qquad (7)$$

where ν_j are the vibrational frequencies. The first term thus represents the vibrational zero-point contributions to the enthalpy, while the second term represents the vibrational entropic contributions from a given lattice model.

Finite temperature/pressure defect concentrations are calculated from the defect formation energies according to

$$\frac{[\text{defect}]}{N_{\text{s,defect}}} = N_{\text{c,defect}} \exp\left(-\frac{\Delta G_{\text{defect}}^{\text{f}}(T,P)}{k_{\text{b}} T}\right) \qquad (8)$$

where $N_{\text{s,defect}}$ is the concentration of defect sites on which the defect may form (for instance concentration of $O_O^{\times}$) and $N_{\text{c,defect}}$ is the number of configurations per site the defect may attain.[36,37] Finally, for each lattice site, the concentration of species (*i.e.*, defects and perfect occupants) must equal the concentration of lattice sites.

5 Results and discussion

5.1 Thermogravimetric measurements

Fig. 1 displays the concentration of water in $RE_2Sn_2O_7$ (RE = La, Sm and Er) as a function of inverse temperature determined from TG measurements in wet air (p_{H_2O} = 0.025 atm). The water uptake increases with decreasing temperature, reflecting the exothermic nature of the hydration reaction (eqn (1)). In the case of $La_2Sn_2O_7$ nominally substituted with 0.20 mol Ca per mol oxide, the water concentration levels off at temperatures below ~450 °C attaining a constant value of ~0.042 mol H_2O per mol oxide, or 0.084 mol $OH_O^{\bullet}$ per mol oxide. Given that thermal equilibrium is reached at the lower temperatures, this saturation reflects the limiting electroneutrality $[Ca_{RE}^{'}] = [OH_O^{\bullet}]$, and thus an effective acceptor concentration of 0.084 mol Ca per mol oxide. This observation is in line with the segregation of $CaSnO_3$ observed in the XRD diffractograms (not shown here) indicating that the nominal acceptor concentration is beyond the solubility limit. We note that Eurenius *et al.*,[18] for $Sm_2Sn_2O_7$ substituted with 0.08 mol Ca per mol oxide, determined the proton concentration to be ~0.04 mol $OH_O^{\bullet}$ per mol oxide at 300 °C, a factor of 2 lower than what we observe here. This deviation could either reflect precipitation of the acceptor, or an unsaturated material due to a non-equilibrium state in the measurements of Eurenius *et al*. Further, at a given temperature (in the unsaturated regime), the water uptake increases in the order Er → → Sm → La, and $La_2Sn_2O_7$ and $Sm_2Sn_2O_7$, moreover, are saturated to higher temperatures than $Er_2Sn_2O_7$, thus

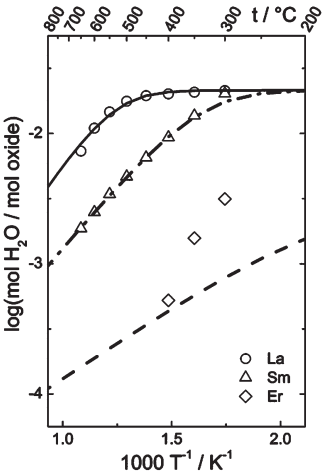

Fig. 1 Water uptake in Ca doped $RE_2Sn_2O_7$ (RE = La, Sm and Er) as a function of inverse temperature in wet air. The symbols represent the water uptake as measured by means of TG, while the lines correspond to curve fitting of the data according to eqn (10).

indicating an effect of the RE ion on the hydration thermodynamics, in line with Eurenius *et al.*[17]

Water uptake in nominally acceptor doped systems can be explained by a simplified defect model where water dissolves according to the reaction in eqn (1) with the acceptor concentration, $[Ca'_{RE}]$, thus being charge-compensated according to the simplified electroneutrality

$$2[v_O^{\bullet\bullet}] + [OH_O^{\bullet}] = [Ca'_{RE}] \tag{9}$$

The hydration thermodynamics corresponding to the measured water uptake may be quantified by the mass action law

$$K_{hydr} = \frac{\left([OH_O^{\bullet}]/N_{s,OH_O^{\bullet}} N_{c,OH_O^{\bullet}}\right)^2}{\left([v_O^{\bullet\bullet}]/N_{s,v_O^{\bullet\bullet}} N_{c,v_O^{\bullet\bullet}}\right)\left([O_O^{\times}]/N_{s,O_O^{\times}}\right)(p_{H_2O}/p^o)} = \exp\left(\Delta_{hydr}S^o/R\right)\exp\left(-\left(\Delta_{hydr}H^o/RT\right)\right) \tag{10}$$

where $N_{s,i}$ and $N_{c,i}$ are the concentration of defect sites and number of configurations per site, respectively, as in eqn (8). As both oxygen vacancies and hydroxide defects mainly are located on the O48f site (see section 5.2) of which there are 6 per formula unit, $N_{s,i}$ equals 6 mol per mol oxide for both defects (for small defect concentrations). Further, there is only one possible vacancy configuration per oxygen site, *i.e.* $N_{c,v_O^{\bullet\bullet}} = 1$. Our DFT calculations (and those of Björketun *et al.*[16]) show that there are two possible orientations of the hydroxide defect (or two low energy H positions) per O48f ion such that $N_{c,OH_O^{\bullet}} = 2$. Finally, $[O_O^{\times}]/N_{s,O_O^{\times}}$ is taken as unity. A combination of eqn (9) and (10) yields the proton concentration

$$[OH_O^{\bullet}] = \frac{K_{hydr} N_{s,v_O^{\bullet\bullet}} N_{c,v_O^{\bullet\bullet}}}{4\left(N_{s,OH_O^{\bullet}} N_{c,OH_O^{\bullet}}\right)^2}\left(\frac{p_{H_2O}}{p^o}\right) \times \left(-1 + \sqrt{1 + \frac{8\left(N_{s,OH_O^{\bullet}} N_{c,OH_O^{\bullet}}\right)^2 [Ca'_{RE}]}{K_{hydr} N_{s,v_O^{\bullet\bullet}} N_{c,v_O^{\bullet\bullet}} (p_{H_2O}/p^o)}}\right) \tag{11}$$

The standard enthalpy and entropy of hydration of the $RE_2X_2O_7$ series were obtained by curve fitting eqn (11) to the TG profiles, with $[Ca'_{RE}]$ = 0.084 mol per mol oxide as a first approximation. The fitted curves are included in Fig. 1 and the extracted hydration enthalpies of Ca-doped $RE_2Sn_2O_7$ for RE = La, Sm and Er equal −103 ± 5, −76 ± 8 and −44 ± 10 kJ mol^{-1}, respectively.

5.2 First principles defect calculations

General defect chemistry of pyrochlores. The defect chemistry of acceptor doped pyrochlores depends on the relative formation energies of the aforementioned defects, where the concentrations must follow the electroneutrality condition (*i.e.*, the complete form of eqn (9))

$$2[v_{O48f}^{\bullet\bullet}] + 2[v_{O8b}^{\bullet\bullet}] + [OH_{O48f}^{\bullet}] + [OH_{O8b}^{\bullet}] = [OH'_{i8a}] + 2[O''_{i8a}] + [A']$$ (12)

where A' is a frozen-in acceptor and the defect concentrations are obtained from their formation energies through eqn (8). Fig. 2 displays the equilibrium defect formation energies (with reference at the equilibrium Fermi level) at 800 K with p_{H_2O} =

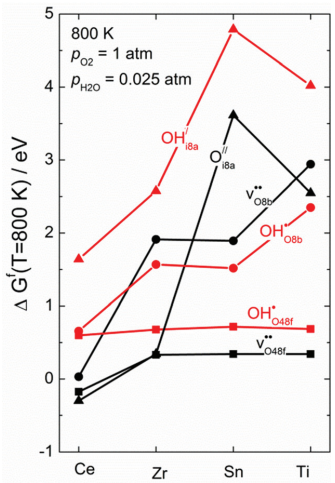

Fig. 2 Equilibrium defect formation energies in the series $Sm_2X_2O_7$ (X = Ti, Sn, Zr and Ce) at 800 K, p_{H_2O} = 0.025 atm and p_{O_2} = 1 atm as obtained when solving the electroneutrality with $[A']$ = 0.084 mol per mol oxide.

0.025 atm and p_{O_2} = 1 atm for the series $Sm_2X_2O_7$ (X = Ti, Sn, Zr and Ce) with a modest acceptor concentration of 0.084 mol per mol oxide. The most prominent change through the series is the stabilisation of the two interstitial defects (O''_{i8a} and OH'_{i8a}), and the two defects at the O8b site ($OH^{\bullet}_{O8b}$ and $v^{\bullet\bullet}_{O8b}$) with increasing size of the X site cation (or decreasing r_{RE}/r_X). This is in agreement with earlier computational studies which have claimed that the stability of anti-Frenkel pairs increases with decreasing r_{RE}/r_X.[38,39] The formation energies indicate that such defects are in complete minority in $Sm_2Ti_2O_7$, while they will be significantly more prominent in $Sm_2Ce_2O_7$ where they even display negative equilibrium formation energies (which correspond to saturation of the defect site). Hence, while defect formation mainly occurs on the O48f site for larger r_{RE}/r_X, pyrochlores with more similar cations display a large degree of anion disorder and occupation of the different oxygen sites, for instance in the cerates, is close to indistinguishable. However, the effect of order/disorder on hydration properties is outside the scope of the present study and is covered in ref. 27 and 40. Fig. 3 displays the computationally estimated defect concentrations in $Sm_2Sn_2O_7$ and $Sm_2Zr_2O_7$ as a function of inverse temperature with p_{H_2O} = 0.025 atm and p_{O_2} = 1 with [A'] = 0.084 mol per mol oxide. As elaborated in the preceding paragraph, the most notable difference is the stabilisation of the O''_{i8a} in $Sm_2Zr_2O_7$ compared to $Sm_2Sn_2O_7$, which manifests itself in a dominating anti-Frenkel disorder at the highest temperatures. At lower temperatures however, these defects are predicted to be in minority with respect to the frozen-in acceptors. The dominating positive defects are in all cases $v^{\bullet\bullet}_{O48f}$ and/or $OH^{\bullet}_{O48f}$ which charge-compensate the acceptor according to eqn (9). The concentration of $OH^{\bullet}_{O48f}$ increases with decreasing temperature and the materials are predicted to saturate and be completely dominated by $OH^{\bullet}_{O48f}$ at the lowest temperatures, in agreement with the TG measurements (see Fig. 1). Finally, protons are predicted to dominate up to slightly higher temperatures in $Sm_2Zr_2O_7$ compared to $Sm_2Sn_2O_7$ (see Fig. 3).

Hydration enthalpy trends through the $RE_2X_2O_7$ series. The dominance of protons or oxygen vacancies is given by their relative formation energies, which may be quantified by the enthalpy of the hydration reaction (eqn (1)). Computationally, the hydration enthalpy is obtained through

$$\Delta_{hydr}H = 2\Delta H^{f}_{OH^{\bullet}_{O48f}} - \Delta H^{f}_{v^{\bullet\bullet}_{O48f}} \quad (13)$$

Note that the enthalpies calculated according to eqn (13) are purely of electronic nature and thus neglect zero-point vibrational contributions. Fig. 4 presents the calculated $\Delta_{hydr}H$ as a function of the ionic radius of the RE ion (RE = La–Lu) through the $RE_2X_2O_7$ series (X = Ti, Sn, Zr and Ce) when constraining the structure to that of an ordered pyrochlore. Within each X ion series, the hydration enthalpy increases (less negative) with decreasing size of the RE cation, *i.e.*, in the order La → Lu. Hence, the $RE_2X_2O_7$ oxides with the larger RE ions will be dominated by protons to higher temperatures than those with the smaller RE ions, in good agreement with the TG measurements. Changing the X site ion has less impact; the hydration enthalpy increases only slightly in the order Ti, Zr → Sn → Ce.

Vibrational contributions to the hydration thermodynamics. The solid state vibrational contributions to the hydration

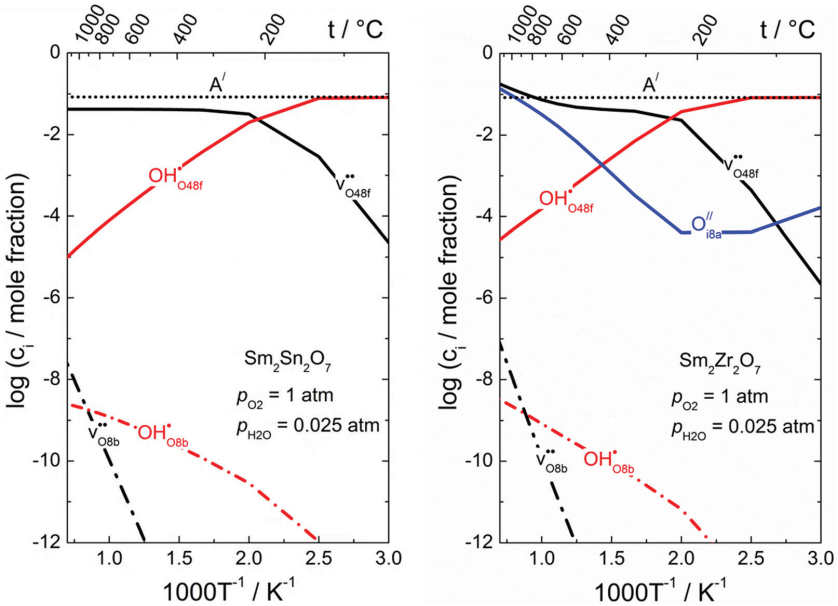

Fig. 3 Thermal equilibrium defect concentrations under wet, oxidising conditions (p_{H_2O} = 0.025 and p_{O_2} = 1 in $Sm_2Sn_2O_7$ and $Sm_2Zr_2O_7$ with [A'] = 084 mol per mol oxide.

thermodynamics may be assumed to be dominated by the creation of 3 additional lattice modes upon formation of each $OH^{\bullet}_{O48f}$ defect (one O–H stretch and two O–H wag modes) and the 3 lattice modes upon filling of a $v^{\bullet\bullet}_{O48f}$ (given by the vibrational modes of a single O48f atom). We thus neglect changes in the vibrational modes of the surrounding atoms, as these contributions have been shown to be small.[41] With the free energy of each vibrational mode given by eqn (7) and by accounting for the zero-point energy of $H_2O(g)$, the Gibbs energy of hydration is obtained through (under $p_{H_2O} = 1$ bar)

$$\begin{aligned}\Delta_{hydr}G^{\circ}(T) = \Delta_{hydr}H \\ &+ 2\left\{\sum_{i=1}^{3}\frac{h\nu_{j,OH^{\bullet}_{O48f}}}{2} + k_bT\ln\left[1-\exp\left(-\frac{h\nu_{j,OH^{\bullet}_{O48f}}}{k_bT}\right)\right]\right\} \\ &+ \left\{\sum_{i=1}^{3}\frac{h\nu_{j,O^{x}_{O}}}{2} + k_bT\ln\left[1-\exp\left(-\frac{h\nu_{j,O^{x}_{O}}}{k_bT}\right)\right]\right\} \\ &- \left\{\sum_{i=1}^{3}\frac{h\nu_{j,H_2O}}{2} + H_{H_2O}(T) - S_{H_2O}(T)\right\}\end{aligned} \quad (14)$$

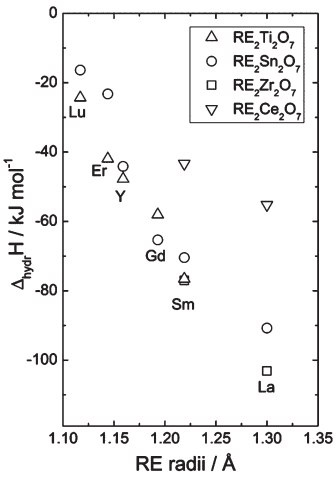

Fig. 4 Calculated hydration enthalpies (excluding zero-point vibrational contributions) for selected pyrochlore structured $RE_2X_2O_7$ compositions (X = Ti, Sn, Zr and Ce).

where the values of ν_{j,H_2O} are taken as those obtained in our DFT calculations: 3840, 3730 and 1585 cm^{-1}. Linearisation of eqn (14) *vs.* T yields the average standard hydration enthalpy and entropy ($\Delta_{hydr}H^{o}$ and $\Delta_{hydr}S^{o}$). $\Delta_{hydr}H^{o}$ derived from eqn (14), consequently, contains zero-point contributions from H_2O and the additional lattice modes, and a contribution due to $H_{H_2O}(T)$, in addition to the electronic part, $\Delta_{hydr}H$, from the preceding section. $\Delta_{hydr}S^{o}$ is similarly composed of the entropy of $H_2O(g)$ itself and the contributions due to excitation of the included lattice modes.

Table 1 lists the calculated vibrational frequencies of the $OH^{\bullet}_{O48f}$ defect and those of an O48f atom in selected $RE_2X_2O_7$ compositions, as well as the corresponding $\Delta_{hydr}H^{o}$ and $\Delta_{hydr}S^{o}$, compared with $\Delta_{hydr}H$ from the preceding section. For all compositions, the $\Delta_{hydr}H^{o}$ is somewhat less exothermic than $\Delta_{hydr}H$ due to inclusion of zero-point energies, but the difference is similar for all compositions due to the minor changes in the vibrational frequencies through the series. Further, the $\Delta_{hydr}S^{o}$ is in the lower limit of the average value of -120 ± 40 J mol^{-1} K^{-1} as usually found experimentally for similar oxides, which may reflect the simplifications of the model. Nevertheless, all entropies are less negative than -215.15 J mol^{-1} K^{-1} as obtained when neglecting all solid state contributions in eqn (14), showing the significance of such contributions in the hydration reaction. There is only a minor change in the entropies through the series due to small changes in the vibrational frequencies, which again reveals only minor structural changes through the series. From eqn (14), the low-frequency modes, *i.e.* the O48f modes and the two O–H wag modes, dominate the solid state vibrational contributions to $\Delta_{hydr}S^{o}$. While the two O–H wag modes are comparable for different series of oxides, the O modes are more dependent on the bonding environment and structure. Hence, we suggest that the hydration entropy is comparable for structurally similar oxides without large symmetry changes (*e.g.* within the pyrochlore series) while it may vary more bet5ween different structural classes (*e.g.* pyrochlore *vs.* monazite). Consequently, the major change in the hydration thermodynamics through the pyrochlore series is $\Delta_{hydr}H$, which we will elaborate upon further in the following section.

Effect of bonding and electronic structure on defect stability. As formation of both $OH^{\bullet}_{O48f}$ and $v^{\bullet\bullet}_{O48f}$ represents forming and breaking various bonds, the individual contributions to the hydration enthalpy may be addressed from changes in the site projected electronic density of states (DOS) upon defect formation.

Table 1 Calculated vibrational frequencies of modes corresponding to the $OH^{\bullet}_{O48f}$ defect and an O48f atom, $\Delta_{hydr}H$ as reported in Fig. 4, and $\Delta_{hydr}H^{o}$ and $\Delta_{hydr}S^{o}$ as obtained through linearisation of eqn (14)

	$OH^{\bullet}_{O48f}$/cm^{-1}			O48f/cm^{-1}			$\Delta_{hydr}H$ kJ mol^{-1}	$\Delta_{hydr}H^{o}$ kJ mol^{-1}	$\Delta_{hydr}S^{o}$ J mol^{-1} K^{-1}
	ν_1	ν_2	ν_3	ν_1	ν_2	ν_3			
$Sm_2Zr_2O_7$	3531	826	719	590	320	312	−77	−68	−165
$Sm_2Ti_2O_7$	3410	829	780	533	344	306	−77	−68	−166
$Sm_2Sn_2O_7$	3431	998	771	579	370	283	−70	−60	−168
$Er_2Sn_2O_7$	3471	980	790	623	372	297	−23	−12	−170
$La_2Sn_2O_7$	3471	980	790	623	372	297	−91	−82	−167

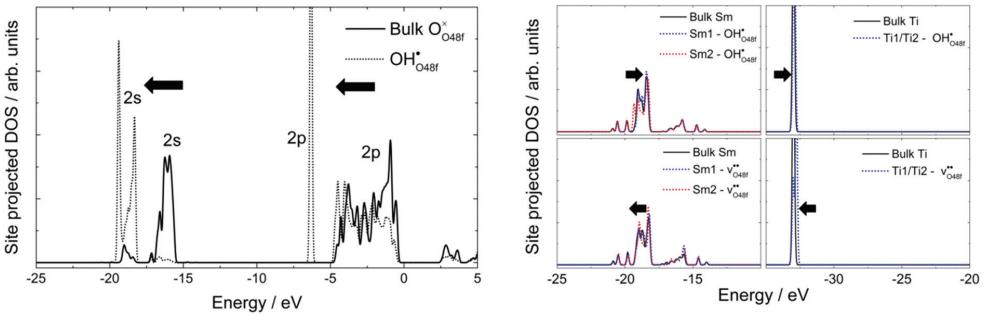

Fig. 5 Site projected DOS in $Sm_2Ti_2O_7$ for (a) $O_O^{\times}$ and $OH_O^{\bullet}$ and (b) cations in bulk and on sites next to $OH_O^{\bullet}$ and $v_O^{\bullet\bullet}$, respectively. The valence band top is set to 0 eV.

Table 2 'Band energies' of various contributions to the hydration enthalpy from integration of the partial DOS; inclusion of H bonding states (E_H), downward shift of O48f states upon OH formation (ΔE_{O48f}), shifts in RE (ΔE_{RE}) and X (ΔE_X) states due to $OH_{O48f}^{\bullet}$ formation and filling of $v_{O48f}^{\bullet\bullet}$, the energy gain of filling a $v_{O48f}^{\bullet\bullet}$ (energy of an O48f ion, ΔE_{O48f}) and the sums of the contributions from the two defects and the corresponding $\Delta_{hydr}H^{band}$.

	Formation of $OH_{O48f}^{\bullet}$ (×2)/eV					Filling of $v_{O48f}^{\bullet\bullet}$/eV				
	E_H	ΔE_{O48f}	ΔE_{RE}	ΔE_X	Sum	E_{O48f}	ΔE_{RE}	ΔE_X	Sum	$\Delta_{hydr}H^{band}$/eV
$Lu_2Ti_2O_7$	−5.4	−7.0	−0.1	+1.4	−11.1	−18.6	−1.4	+0.2	−19.9	−42.0
$Er_2Ti_2O_7$	−5.4	−7.1	−0.1	−0.6	−13.0	−18.6	−0.6	−1.3	−20.5	−46.5
$Sm_2Ti_2O_7$	−5.4	−7.6	−0.5	+0.1	−13.3	−20.8	−1.8	−0.8	−23.4	−50.0
$Sm_2Sn_2O_7$	−5.0	−10.9	+1.4	−5.2	−19.6	−25.1	+1.9	+13.8	−9.4	−48.6
$Sm_2Zr_2O_7$	−6.2	−9.1	−0.4	−0.4	16.1	−17.8	−1.8	+2.4	−17.2	−49.4
$Sm_2Ce_2O_7$	−5.4	−8.9	+0.2	−0.5	−14.7	−15.3	−2.3	+4.8	−12.8	−42.2

As illustrated in Fig. 5 for $Sm_2Ti_2O_7$, $OH_{O48f}^{\bullet}$ formation and $v_{O48f}^{\bullet\bullet}$ consumption result in:

– Inclusion of H bonding states (Fig. 5a) – 'E_H' in Table 2.
– Stabilisation of the O48f ions as represented by the downward shift in O48f states upon O–H bond formation (Fig. 5a) – 'ΔE_{O48f}' in Table 2.
– Filling of $v_{O48f}^{\bullet\bullet}$ which is represented by the bulk O48f bonding states in Fig. 5a – 'E_{O48f}' in Table 2.
– Shift in nearest neighbour RE and X ion states upon $OH_{O48f}^{\bullet}$ formation and $v_{O48f}^{\bullet\bullet}$ consumption (Fig. 5b) –'ΔE_{RE}' and 'ΔE_X' in Table 2.

These contributions may be quantified by changes in the 'band energy' as obtained by integration of the partial DOS, E_i^{DOS}, for given ions

$$E_i^{DOS} = \sum_{\varepsilon_i=-\infty}^{\varepsilon_i=\varepsilon_{VBM}} D(\varepsilon_i)\varepsilon_i \Delta\varepsilon \qquad (15)$$

where $D(\varepsilon_i)$ is the calculated DOS at energy ε_i. Table 2 summarises the resulting band energies of the different contributions. The trend in the $\Delta_{hydr}H^{band}$ matches the trend of $\Delta_{hydr}H$; the enthalpies become less exothermic with decreasing RE radii, and only slightly less exothermic in the order Ti, Zr → Sn → Ce. The individual contributions indicate that these changes are due to variations in the stability of both $OH_{O48f}^{\bullet}$ and $v_{O48f}^{\bullet\bullet}$. In the series Sm → Er → Lu, both the energy gain of forming two $OH_{O48f}^{\bullet}$ and that of filling the $v_{O48f}^{\bullet\bullet}$ decrease (*i.e.*, less stable protons and more stable oxygen vacancies with decreasing RE size). The variation is mostly due to a decreasing contribution from ΔE_{O48f} (*i.e.*, the stabilisation of the O ions by bonding to H) and E_{O48f} (*i.e.*, stability of O48f ions). However, upon changing the X site ion, variations in the different contributions are to some extent counteracting. The energy gain of forming two $OH_{O48f}^{\bullet}$ increases (less stable protons) in the order Sn → Zr → Ce → Ti, whereas that from filling a $v_{O48f}^{\bullet\bullet}$ increases (less stable vacancies) in the order Sn → Ce → Zr → Ti. Overall, this results in a less pronounced overall effect on the hydration enthalpy. The fact that ΔE_{O48f} and E_{O48f} vary in a concise manner through the RE ion series indicates that these contributions and variations in the hydration enthalpy through the series may be related to shifts in the bonding nature (degree of ionicity) and stability of the O48f ions (or stability of the oxide). The effects of changing the X site ion seem less conclusive and such factors vary and affect the defect stability and hydration thermodynamics in a more complicated manner.

Bonding nature. Table 3 lists the Bader charges of the RE, X, O8b and O48f ions for selected $RE_2X_2O_7$ compositions as emerging from the Bader partitioning of the bulk systems. Within the $RE_2Ti_2O_7$ series, the charge of the RE cation increases while that of the two oxide ions becomes more negative in the order Sm → Lu, thus indicating increased ionic character through the series, in line with the predictions by for instance Kennedy *et al.*[42] There is a similar effect of changing the X ion; the X site

Table 3 Bader charges of selected pristine $RE_2X_2O_7$ compositions

	RE	X	O8b	O48f
$Lu_2Ti_2O_7$	2.28	2.35	−1.66	−1.30
$Er_2Ti_2O_7$	2.27	2.34	−1.65	−1.29
$Sm_2Ti_2O_7$	2.16	2.34	−1.37	−1.27
$Sm_2Sn_2O_7$	2.18	2.46	−1.38	−1.31
$Sm_2Zr_2O_7$	2.18	2.57	−1.39	−1.35

ions become more positive and the O48f ions become more negative in the order Ti → Sn → Zr, while there is only a minor change in the Sm and O8b ions, indicating increasing ionic character of the X–O48f bond. Further, the change in the O48f ion polarisation upon X site ion substitution is approximately twice that of the change from La to Lu.

In the literature, one of the hypotheses has been that the hydration enthalpy correlates with the basicity of the oxides.[1,6] The basicity, and therefore in principle also $\Delta_{hydr}H^o$, should correlate with the Bader charges of the O48f ions. However, we do not observe any such simple correlation in this work (Fig. 4 and Table 3). Interestingly, the change in the Bader charge of the O48f ion is most pronounced upon changing the X ion, or opposite to the change in $\Delta_{hydr}H^o$. Further, from the band energies in the preceding section (see Table 2), it is clear that the $\Delta_{hydr}H^o$ trend from La → Lu is due both to destabilisation of protons and stabilisation of vacancies, which thus mainly may be attributed to the decreasing oxide stability through the RE series. Similarly, upon changing the X site ion, the defects are affected by stabilisation of the oxide ions, but the effect is to some extent counteracted by the more pronounced shift in the degree of ionicity and O48f polarisation, and the $\Delta_{hydr}H^o$ thus varies in a more complex manner upon changing the X site ion.

5.3 General hydration trends

As elaborated in the preceding section, the hydration enthalpy of $RE_2X_2O_7$ pyrochlores for a given X ion correlates with the size of the RE ion, which is attributed to destabilisation of the oxide and increasing degree of ionicity for smaller RE ions. Fig. 6 displays the obtained hydration enthalpies *versus* the calculated oxide formation enthalpies and the r_{RE}/r_X ratio, respectively. There is no clear trend in either the formation enthalpy or in the r_{RE}/r_X ratio that applies to all series. However, within a given X-ion series, the hydration enthalpy clearly correlates with both parameters, as both reflect the stability and bonding nature of the oxides.

The hydration enthalpy of rare-earth pyrochlores displays the opposite dependence on the RE ion compared to rare-earth sesquioxides (RE_2O_3)[2] and rare-earth ortho-niobates ($RENbO_4$).[10] This may indicate larger changes in the O ion polarisation upon reduction of the RE ion size in the two latter series than in the pyrochlores. Nevertheless, also in these systems, changing the X ion has a smaller effect on the hydration properties than the RE ion (*e.g.* $LaPO_4$, $LaAsO_4$ and $LaVO_4$)[8,9] which as for the pyrochlores can be due to counteracting effects from changes in O ion polarisation and stability of the oxides.

For ABO_3 perovskite oxides, the hydration enthalpy has been correlated with the difference in electronegativity of the A and B

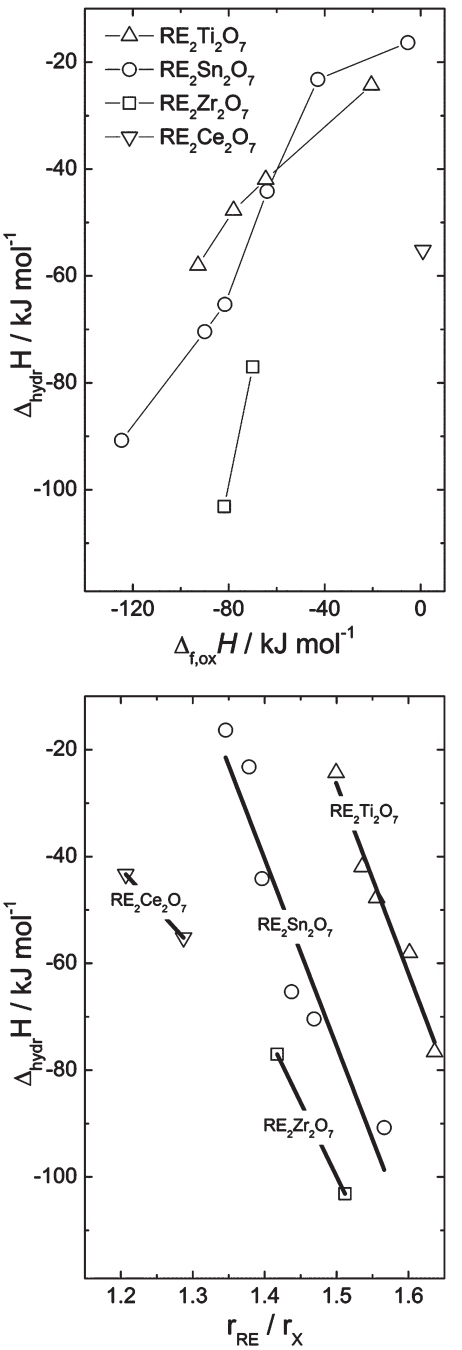

Fig. 6 Hydration enthalpies *versus* the formation enthalpy (from DFT calculations) and *versus* the r_{RE}/r_X ratio of the $RE_2X_2O_7$ (X = Ti, Sn, Zr and Ce) pyrochlore oxides.

cations[1,20] and related to the basicity of the oxide ions. As elaborated in this study, this trend may rather reflect changes in the oxide stability and degree of ionicity, which also depends on the electronegativity of the two cations. A detailed study of the stabilisation of protons and oxygen vacancies with bonding nature and stability of the oxides through different classes of oxides will be pursued to elaborate on more general hydration trends.

6 Summary

Comparative DFT calculations and TG measurements have been employed to elucidate the trends in the defect chemistry and hydration properties through the pyrochlore structured $RE_2X_2O_7$ (RE = La–Lu and X = Ti, Sn, Zr and Ce) series of compounds. The DFT calculations reveal that, in systems with large r_{RE}/r_X, the dominating positive defects are $v_{O48f}^{\bullet\bullet}$ and/or $OH_{O48f}^{\bullet}$ which charge-compensate acceptor dopants. In systems with smaller r_{RE}/r_X, however, the interstitial defects O_{i8a}'' and OH_{i8a}', and defects at the second oxygen site, $OH_{O8b}^{\bullet}$ and $v_{O8b}^{\bullet\bullet}$, are stabilised, and such oxides therefore display a large degree of anion disorder.

Total energy and phonon calculations within the DFT approximation reveal that trends in the hydration thermodynamics through the pyrochlore series to a large extent are dominated by electronic (binding) contributions. Hydration entropies obtained from phonon calculations and a simplified Boltzmann model are comparable for all included series due to only small changes in the vibrational characteristics of oxygen ions and protons. The hydration enthalpies obtained with DFT calculations become more exothermic with increasing size of the RE ion, while the effect of changing the X site element is smaller. These computational findings are in good agreement with TG measurements on Ca doped $RE_2Sn_2O_7$ (RE = La, Sm and Er), which show increasing water uptake (at a given temperature) and more exothermic hydration enthalpies with increasing RE ion size. The relative contributions from formation of protons and filling of oxygen vacancies to the hydration enthalpy were quantified by integration of the calculated partial DOS. The increasing hydration enthalpy with decreasing RE ion size is attributed to destabilisation of protons and stabilisation of oxygen vacancies, *i.e.*, additive contributions, through the series. This stabilisation is related to both increasing stability of the oxide and increasing degree of ionicity in the same order. The smaller effect of changing the X site element is similarly explained by counteracting contributions from stabilisation of both protons and oxygen vacancies. Hence, within each X ion series, the hydration enthalpies correlate with the size of the RE ion, or the r_{RE}/r_X ratio, while no general trend applying to all series was found.

References

1 T. Norby, M. Widerøe, R. Gløckner and Y. Larring, *Dalton Trans.*, 2004, 3012–3018.
2 Y. Larring and T. Norby, *Solid State Ionics*, 1995, **77**, 147–151.
3 K. D. Kreuer, *Solid State Ionics*, 1999, **125**, 285–302.
4 H. G. Bohn and T. Schober, *J. Am. Ceram. Soc.*, 2000, **83**, 768–772.
5 K. D. Kreuer, S. Adams, W. Münch, A. Fuchs, U. Klock and J. Maier, *Solid State Ionics*, 2001, **145**, 295–306.
6 K. D. Kreuer, *Annu. Rev. Mater. Res.*, 2003, **33**, 333–359.
7 T. Norby and N. Christiansen, *Solid State Ionics*, 1995, **77**, 240–243.
8 M. Huse, T. Norby and R. Haugsrud, *J. Electrochem. Soc.*, 2011, **158**, B857–B865.
9 T. S. Bjørheim, T. Norby and R. Haugsrud, *J. Mater. Chem.*, 2012, 22.
10 R. Haugsrud and T. Norby, *Nat. Mater.*, 2006, **5**, 193–196.
11 R. Haugsrud and T. Norby, *Solid State Ionics*, 2006, **177**, 1129–1135.
12 T. Shimura, M. Komori and H. Iwahara, *Solid State Ionics*, 1996, **86–8**, 685–689.
13 T. Omata, K. Okuda, S. Tsugimoto and S. Otsuka-Matsuo-Yao, *Solid State Ionics*, 1997, **104**, 249–258.
14 T. Omata and S. Otsuka-Yao-Matsuo, *J. Electrochem. Soc.*, 2001, **148**, E252–E261.
15 T. Omata, K. Ikeda, R. Tokashiki and S. Otsuka-Yao-Matsuo, *Solid State Ionics*, 2004, **167**, 389–397.
16 M. E. Björketun, C. S. Knee, B. J. Nyman and G. Wahnström, *Solid State Ionics*, 2008, **178**, 1642–1647.
17 K. E. J. Eurenius, E. Ahlberg and C. S. Knee, *Solid State Ionics*, 2010, **181**, 1258–1263.
18 K. E. J. Eurenius, E. Ahlberg and C. S. Knee, *Dalton Trans.*, 2011, **40**, 3946–3954.
19 T. Tauer, R. O'Hayre and J. W. Medlin, *Solid State Ionics*, 2011, **204–205**, 27–34.
20 T. S. Bjørheim, A. Kuwabara, I. Ahmed, R. Haugsrud, S. Stølen and T. Norby, *Solid State Ionics*, 2010, **181**, 130–137.
21 T. Norby and Y. Larring, *Curr. Opin. Solid State Mater. Sci.*, 1997, **2**, 593–599.
22 H. Fjeld, R. Haugsrud, A. E. Gunnæs and T. Norby, *Solid State Ionics*, 2008, **179**, 1849–1853.
23 J. Lian, K. B. Helean, B. J. Kennedy, L. M. Wang, A. Navrotsky and R. C. Ewing, *J. Phys. Chem. B*, 2006, **110**, 2343–2350.
24 M. Dorogova, A. Navrotsky and L. A. Boatner, *J. Solid State Chem.*, 2007, **180**, 847–851.
25 J. A. Díaz-Guillén, M. R. Díaz-Guillén, K. P. Padmasree, A. F. Fuentes, J. Santamaría and C. León, *Solid State Ionics*, 2008, **179**, 2160–2164.
26 P. K. Moon, *PhD Thesis, Electrical Conductivity and Structural Disorder in $Gd_2Ti_2O_7$-$Gd_2Zr_2O_7$ and $Y_2Ti_2O_7$-$Y_2Zr_2O_7$ Solid Solutions*, Department of Materials Science and Engineering, Massachusetts Institute of Technology, Cambridge, MA, 1988.
27 V. Besikiotis, S. Ricote, M. H. Jensen, T. Norby and R. Haugsrud, *Solid State Ionics*, 2012, accepted.
28 E. Reynolds, P. E. R. Blanchard, Q. Zhou, B. J. Kennedy, Z. Zhang and L.-Y. Jang, *Phys. Rev. B*, 2012, **85**, 132101.
29 G. Kresse and J. Furthmüller, *Phys. Rev.B*, 1996, **54**, 11169.
30 G. Kresse and D. Joubert, *Phys. Rev. B*, 1999, **59**, 1758.
31 J. P. Perdew, K. Burke and M. Ernzerhof, *Phys. Rev. Lett.*, 1996, **77**, 3865.
32 P. E. Blöchl, *Phys. Rev. B*, 1994, **50**, 17953.
33 G. Henkelman, A. Arnaldsson and H. Jónsson, *Comput. Mater. Sci.*, 2006, **36**, 354–360.
34 T. Mattila and A. Zunger, *Phys. Rev. B*, 1998, **58**, 1367.
35 M. W. Chase Jr., *NIST-JANAF Thermochemical Tables*, The American Institute of Physics for The National Institute of Standards and Technology, New York, 1998.
36 J. Maier, *Physical Chemistry of Ionic Materials: Ions and Electrons in Solids*, John Wiley & Sons LTD, England, 2004.
37 A. Kuwabara, *Sci. Technol. Adv. Mater.*, 2007, **8**, 519.
38 P. J. Wilde and C. R. A. Catlow, *Solid State Ionics*, 1998, **112**, 173–183.
39 L. Minervini, R. W. Grimes and K. E. Sickafus, *J. Am. Ceram. Soc.*, 2000, **83**, 1873–1878.
40 L.-E. Q. Kalland, V. Besikiotis, R. Haugsrud and T. Norby, *Materials Research Society, Spring Meeting*, Materials Research Society, San Francisco, CA, USA, 2012.
41 M. E. Björketun, P. G. Sundell and G. Wahnstrom, *Faraday Discuss.*, 2007, **134**, 247–265.
42 B. J. Kennedy, B. A. Hunter and C. J. Howard, *J. Solid State Chem.*, 1997, **130**, 58–65.

Manuscript II

Crystal structure hydration and ionic conductivity of the inherently oxygen-deficient $La_2Ce_2O_7$

Solid State Ionics, **228**,1-7 (2012)

V. Besikiotis, C. S. Knee, I. Ahmed, R. Haugsrud, T. Norby

Erratum

The correct form of eq. 8 is:

$$[\mathrm{OH}_{\mathrm{O}}^{\bullet}] = \frac{K_{\mathrm{hydr}}\left(N_{\mathrm{s,OH}_{\mathrm{O}}^{\bullet}} N_{\mathrm{c,OH}_{\mathrm{O}}^{\bullet}}\right)^2}{4 N_{\mathrm{s,v}_{\mathrm{O}}^{\bullet\bullet}} N_{\mathrm{c,v}_{\mathrm{O}}^{\bullet\bullet}}} \left(\frac{p_{\mathrm{H_2O}}}{p^{\circ}}\right) \left(-1 + \sqrt{1 + \frac{8 N_{\mathrm{s,v}_{\mathrm{O}}^{\bullet\bullet}} N_{\mathrm{c,v}_{\mathrm{O}}^{\bullet\bullet}} \left[\mathrm{La}_{\mathrm{Ce}}^{/}\right]}{K_{\mathrm{hydr}}\left(N_{\mathrm{s,OH}_{\mathrm{O}}^{\bullet}} N_{\mathrm{c,OH}_{\mathrm{O}}^{\bullet}}\right)^2 \left(\frac{p_{\mathrm{H_2O}}}{p^{\circ}}\right)}} \right)$$

Manuscript III

Conductivity and hydration trends in disordered fluorite and pyrochlore oxides: A study on lanthanum cerate-zirconate based compounds

Solid State Ionics, **229**, 26-32 (2012)

V. Besikiotis, S.Ricote, M.H.Jensen, T. Norby, R. Haugsrud

Manuscript IV

On La_2NiO_4 as cathode on lanthanum tungstate $La_{5.6}WO_{11.4}$ electrolyte

Status: To be submitted

V. Besikiotis, R. Strandbakke, T. Norby

5. Discussion beyond the manuscripts

"So he [Democritus] thinks that they hold to on to one another and remain together up to the time when some stronger force reaches them from their environment and shakes them and scatters them apart"

Aristotle

On Democritus Fragment 208

A common characteristic of the systems investigated in manuscripts II and III is the negligible grain boundary resistance. This characteristic was not discussed in the relevant manuscripts, as it was beyond the scope of each manuscript. In this last part of the thesis I provide an exploratory discussion on the negligible grain boundary resistance of $La_2Ce_2O_7$.

On the grain boundary conductivity of lanthanum cerate

In manuscript II we show that $La_2Ce_2O_7$ in terms of defects and transport behaves as 50% La-doped CeO_2. The deconvolution of the impedance spectra at 400 °C under wet, deuterated, and dry O_2 revealed no grain boundary contribution to the total impedance of the system. On the other hand this is not the case for undoped or moderately doped CeO_2. An early study on the electrical behaviour of acceptor-doped CeO_2 by Gerhardt and Nowick [41], showed that what they called "grain–boundary effect" leads to a greatly reduced ionic dc conductivity for CeO_2 doped up to 6% with La^{3+}, Y^{3+}, Gd^{3+}. The same phenomenon is also observed for other state-of-the-art oxide ion conductors *i.e.* Y-doped

ZrO_2 [42], and proton conductors *i.e.* Ca-$LaNbO_4$ [43], Y-doped $BaZrO_3$ [44-46], and Gd-doped $BaCeO_3$ [47] revealing high grain boundary electrical resistance. Possible applications of these oxides as electrolytes in fuel cells can be limited because of dominating grain boundary resistance.

In the relevant literature two different explanations have been advanced to account for this high resistance: symmetry reduction and space-charge layers. In the former the reduced symmetry of a grain boundary is expected to hinder the migration process, since proton migration in perovskites, which occurs by the Grotthuss mechanism, is known to be sensitive to lattice symmetry [48, 49]. In the latter, the high resistance of the grain boundaries is attributed to an intrinsic effect of negatively charged space-charge layers created in response to the positively charged grain boundary core by accumulation of oxygen vacancies to relieve mismatch stress [50-52]. This charge is compensated by accumulation of acceptor dopants and a depletion of positive defects, including protons, in the adjacent space charge layers (cf. Fig. 5.1). The experimental study of Guo and Waser [53] on the electrical properties of the grain boundaries of acceptor-doped CeO_2 and ZrO_2 provided sound indications that space charge layers are present. In the following I will speculate around the grain boundary conductivity of $La_2Ce_2O_7$ providing in parallel aspects of space-charge layer theory.

From an electrical point of view, a grain boundary consists of a grain boundary core and two adjacent space-charge layers (cf. Fig. 5.1). The grain boundary core is structurally different from the bulk. The intercept between the grain boundary core and the space-charge layer is positioned at $x = 0$. The size of one space-charge layer is given by the space-charge layer width λ^*. The two space-charge layers are, in structural terms, part of the bulk of the crystal. Hence, it is reasonable to assume that the mobility of the charge carriers in the space-charge layer is equal to what we find in the bulk of the crystal. The electroneutral part of the bulk crystal is termed grain interior.

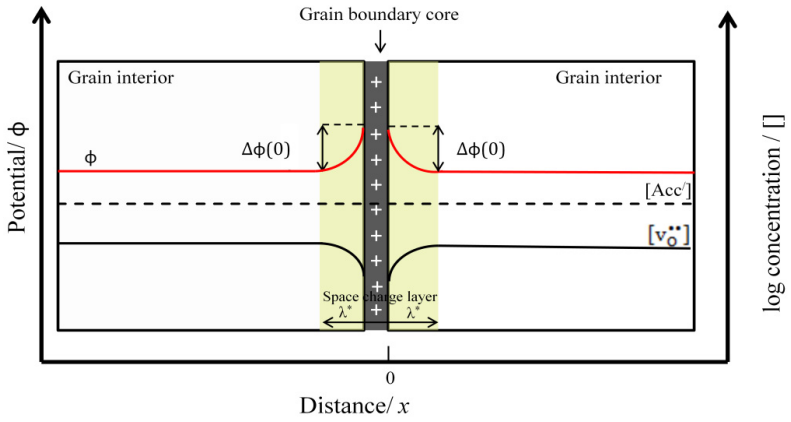

Figure 5.1 Simplified illustration of the space charge layer theory.

The grain boundary core may in principle be positively or negatively charged. In this occasion we assume that the grain boundary core is positively charged, with oxygen vacancies being responsible for this charge. The positively charged core will give rise to charge-compensating layers of so-called space charge around the core. As a result, a non-uniform electrical potential ϕ in the space-charge layers develops. The space-charge potential $\Delta\phi(0)$[10] is the potential at the grain boundary core at $x = 0$ relative to the grain interior at $x = \infty$, $\Delta\phi(0) = \phi(0) - \phi(\infty)$, cf. Fig 5.1. $\Delta\phi(0)$ increases with the excess of oxygen vacancies being transferred to the core. The higher the $\Delta\phi(0)$, the more severe the depletion of the oxygen vacancies in the space-charge layer is. Thus, $\Delta\phi(0)$ phenomenologically scales with the grain boundary resistance.

The formation of a space-charge layer is driven by differences in the standard chemical potential of charged point defects between the grain interior and the grain boundary core:

$$\Delta\mu_i^0 = \mu_{i,\mathrm{c}}^0 - \mu_{i,\mathrm{gi}}^0 \tag{5.1}$$

where c and gi denote grain boundary core $(x = 0)$ and grain interior $(x = \infty)$, respectively. A negative $\Delta\mu_i^0$ indicates that the defect prefers to reside in the grain boundary core. If the defect is mobile, then it will segregate to the grain boundary core,

[10] It is also called the Schottky barrier height.

electrically charging it in the process, forming charge compensating space-charge layers. The system lowers its Gibbs free energy by redistributing defects between grain-boundary core and grain interior, but there is a penalty of having charge separation. The equilibrium corresponds to the minimum in overall Gibbs energy, and with the electrochemical potential of all mobile defects being constant across the grain interior and grain boundary regions (actually the entire sample) [48]. In the case of $La_2Ce_2O_7$, treating it as 50% La-doped CeO_2, there are three defects that may redistribute between the bulk and the core: acceptor-dopants, oxygen vacancies and protons. In the treatment here we consider the Mott-Schottky approximation where the acceptor-dopant cations are immobile. Thus, there are only two thermodynamic driving energies for space charge formation, namely $\Delta\mu^0_{v_0^{\bullet\bullet}}$ and $\Delta\mu^0_{OH_0^{\bullet}}$.

The electrochemical potential of a mobile oxygen vacancy as a function of distance x, assuming unity activity coefficient, is:

$$\eta_{v_0^{\bullet\bullet}}(x) = \mu^0_{v_0^{\bullet\bullet}} + k_B T \ln c_{v_0^{\bullet\bullet}}(x) + e\phi(x) \tag{5.2}$$

where $c_{v_0^{\bullet\bullet}}(x)$ is the volume concentration of oxygen vacancies at position x from the grain boundary core, k_B is the Boltzmann constant and T the temperature. At equilibrium, where $\eta_{v_0^{\bullet\bullet}}(x) = \eta_{v_0^{\bullet\bullet}}(\infty)$, the difference in the electrical potential at position x in the space-charge layer referenced to the potential in the grain interior, $\Delta\phi(x) = \phi(x) - \phi(\infty)$, is given by:

$$\Delta\phi(x) = \frac{k_B T}{e} \ln \frac{c_{v_0^{\bullet\bullet}}(\infty)}{c_{v_0^{\bullet\bullet}}(x)} \tag{5.3}$$

and, consequently:

$$\frac{c_{v_0^{\bullet\bullet}}(\infty)}{c_{v_0^{\bullet\bullet}}(x)} = \exp\left(\frac{e\Delta\phi(x)}{k_B T}\right) \tag{5.4}$$

From the Poisson equation we have:

$$\frac{d^2\Delta\phi(x)}{dx^2} = -\frac{1}{\varepsilon} Q(x) \tag{5.5}$$

where ε is the dielectric permittivity, and $Q(x)$ the net charge density in the space-charge layer at position x. Considering that oxygen vacancies are strongly depleted in the space-charge layer, the net charge density can be considered to be governed by the acceptors:

$$Q(x) = e\left(2c_{\mathrm{v_O^{\bullet\bullet}}} - c_{\mathrm{Acc/}}\right) \approx -ec_{\mathrm{Acc/}} \tag{5.6}$$

substituting eq. 5.6 to 5.5 the Poisson equation reads:

$$\frac{d^2\Delta\phi(x)}{dx^2} = \frac{1}{\varepsilon}ec_{\mathrm{Acc/}} \tag{5.7}$$

By integration of eq. 5.7 (see De Souza *et al.* [48]) one obtains the relationship between $\Delta\phi(0)$, the core charge Q_c, and $c_{\mathrm{Acc/}}$, given by:

$$\Delta\phi(0) = \frac{{Q_c}^2}{8\varepsilon c_{\mathrm{Acc/}}} + \frac{k_{\mathrm{B}}T}{ze} \tag{5.8}$$

Defining the Debye length, L_D, for this case as [46, 54]:

$$L_D = \left(\frac{k_B T\varepsilon}{2e^2 c_{\mathrm{Acc/}}}\right)^{\frac{1}{2}} \tag{5.9}$$

and the effective space-charge layer width, λ^*, as:

$$\lambda^* = 2L_D\left(\frac{e\,\Delta\phi(0)}{k_B T}\right)^{\frac{1}{2}} = \left(\frac{2\varepsilon\,\Delta\phi(0)}{ec_{\mathrm{Acc/}}}\right)^{\frac{1}{2}} \tag{5.10}$$

the concentration of the oxygen vacancies in the space-charge layer at position x will be given by:

$$\frac{c_{\mathrm{v_O^{\bullet\bullet}}}(x)}{c_{\mathrm{v_O^{\bullet\bullet}}}(\infty)} = \exp\left[-\frac{1}{2}\left(\frac{x-\lambda^*}{L_D}\right)^2\right] \tag{5.11}$$

For $x > \lambda^*$, we obviously have $c_{\mathrm{v_O^{\bullet\bullet}}}(\infty) = c_{\mathrm{v_O^{\bullet\bullet}}}(x)$. Similarly the expression for the concentration of protons will read:

$$\frac{c_{OH_0^\bullet}(x)}{c_{OH_0^\bullet}(\infty)} = \exp\left[-\frac{1}{4}\left(\frac{x-\lambda^*}{L_D}\right)^2\right] \quad (5.12)$$

From the formalism presented above it is apparent that systems with lower dopant concentrations are expected to reveal larger space-charge layer effects.

Fig. 5.2 shows the variation of $\Delta\phi(0)$ as a function of dopant concentration based on eq.5.8 at 400 °C. The input value for Q_c was calculated from the $\Delta\phi(0)$ of 10% acceptor doped CeO_2 as reported by Guo and Waser [53]. It is interesting to note that the vertex of the hyperbola appears approximately at 10% doping, and above 30% doping the decrease is less pronounced.

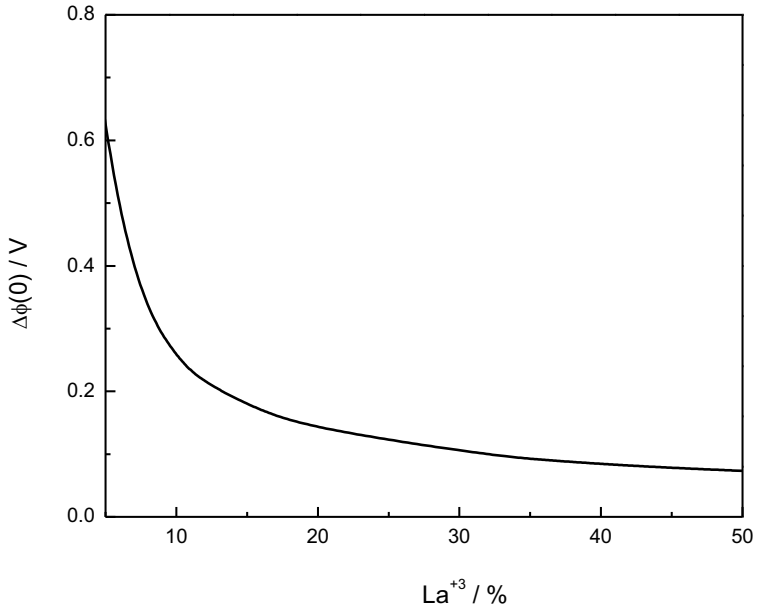

Figure 5.2 The potential at the core, $\Delta\phi(0)$, as a function of La^{3+} doping at 400 °C.

From eq. 5.8 $\Delta\phi(0)$ is 0.25 and 0.07 V for 10 and 50%-La doped CeO_2, respectively. Inserting these values to eq. 5.10 the λ^* for the two doping levels can be obtained. Assuming a defect scenario where oxygen vacancies are charge compensated by the

acceptors, $2c_{v_O^{\bullet\bullet}}(\infty) = c_{Acc/}$, the concentration profile of oxygen vacancies in the space-charge layer at 400 °C, based on eq. 5.11, can be plotted as shown in Fig. 5.3. It is evident from Fig. 5.3 that the decrease of $\Delta\phi(0)$ by increasing the doping level results in a decrease in λ^*, justifying the decrease of the grain boundary resistance with increasing the acceptor doping in CeO_2 as it is reported in literature [41, 55]. Hence, a reasonable assumption to make based on the behaviour of $La_2Ce_2O_7$ as 50%-La doped CeO_2, is that heavy doping dramatically decreases $\Delta\phi(0)$ (cf. Fig. 5.2) and in turn also the grain boundary resistance.

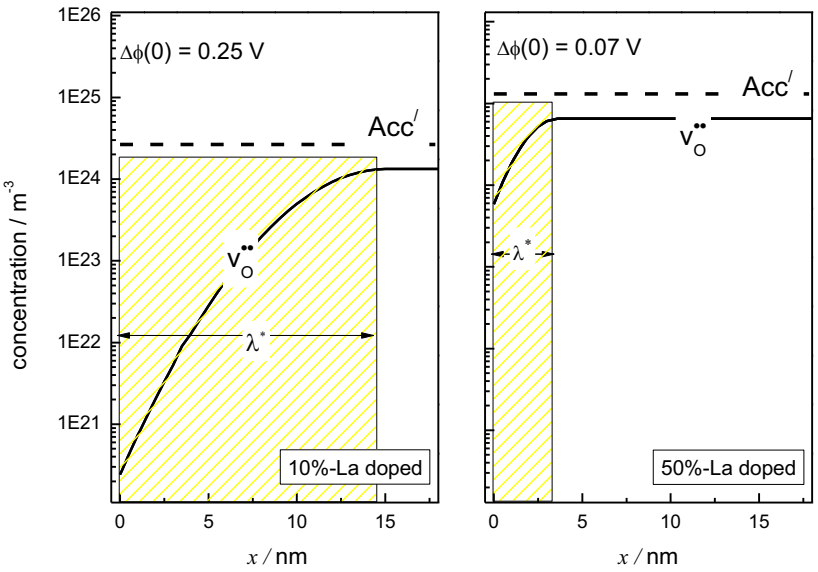

Figure 5.3 λ^* and concentration profiles of oxygen vacancies in the space charge layer for 10 and 50% La doped CeO_2 at 400 °C.

Under wet O_2 ($pH_2O = 0.025$ atm) at 400 °C our findings in manuscript II suggest that protons contribute to the ionic conductivity of $La_2Ce_2O_7$. In this case the electroneutrality condition reads:

$$c_{OH_O^{\bullet}}(\infty) + 2c_{v_O^{\bullet\bullet}}(\infty) = c_{Acc/} \tag{5.13}$$

The impedance spectra recorded at 400 °C shown in Fig.3 in Manuscript II reveal no grain boundary resistance for $La_2Ce_2O_7$ neither in wet nor in dry O_2.

Based on the thermodynamic and transport parameters, reported in manuscript II, the concentration of oxygen vacancies and protons in the grain interior can be obtained, and the concentration profile of oxygen vacancies and protons in the space-charge layer can be plotted, cf. Fig 5.4.

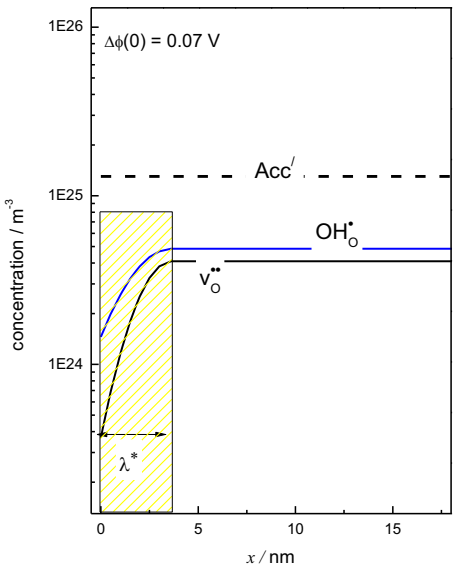

Figure 5.4 λ^* and concentration profiles of oxygen vacancies and protons in the space charge layer of $La_2Ce_2O_7$ at 400 °C and $p\mathrm{H_2O} = 0.025$ atm.

From Fig. 5.4 it is evident that under wet O_2 ($p\mathrm{H_2O} = 0.025$ atm) at 400 °C protons are marginally the main charge carrier both in the grain interior and in the space-charge layer, while the depletion of oxygen vacancies in the space charge layer is more severe due to their double effective charge.

In conclusion the behaviour of $La_2Ce_2O_7$ as 50% La-doped CeO_2 rationalizes the negligible grain boundary resistance attributed to the low $\Delta\phi(0)$ and λ^* stemming from heavy doping.

6. Summary and outlook

"Every man has his own circle composed of trees, animals, men, ideas, and he is in duty bound to save this circle. He, and no one else. If he does not save it, he cannot be saved"

"Free yourself from the simple complacency of the mind that thinks to put all things in order and hopes to subdue phenomena. Free yourself from the terror of the heart that seeks and hopes to find the essence of things"

Nikos Kazantzakis
Ascesis: The saviors of god, 1927

Every generation is confronted with new challenges and new opportunities. Fossil-fuels have offered astounding opportunities to the mankind and especially the rich western world. The technological advances around the utilization of fossil-fuels made energy available to a degree that mankind never experienced before. Now mankind is facing the challenges arising from fossil-fuel exploitation. The proven reserves of fossil-fuels are progressively decreasing, and their continuous use produces harmful effects on humans and the environment [56, 57]. Energy improves people's standard of living, as it is embodied in any type of goods and is needed to produce any kind of service. If we want to decrease the disparity, in terms of quality of life, between developed and developing countries, we have to make energy available and be able to produce it in a sustainable manner. Therefore broadening the spectrum off available and sustainable means of energy production is crucial. This thesis attempted an understanding of the fundamental properties governing the ionic behavior of pyrochlores and disordered fluorite oxides. These oxides can be employed for energy production, namely, as electrolytes and electrode components in PC-SOFCs.

Proton conductivity is a main materials' property that determines the suitability of pyrochlores and disordered fluorite oxides as electrolytes in a PC-SOFC. In these oxides protons are natively neither part of the structure nor of the stoichiometry. They are introduced from the surrounding environment notably hydrogen or water, charge compensating negative defects which are part of the nonstoichiometry or structure of the

material. In that respect hydration thermodynamics and defect chemistry of pyrochlores and disordered fluorite oxides, are of great importance.

In manuscript I with the aid of DFT we elucidated trends in the general defect chemistry and hydration enthalpy of $RE_2X_2O_7$ (RE = La-Lu and X = Ti, Sn, Zr and Ce) series. The hydration of selected compositions was also studied by means of TG, in order to justify the use of DFT calculations. The latter showed that the hydration enthalpy becomes more exothermic with increasing size of RE ion, while the effect is smaller when changing the size of the X ion. These computational findings were in good agreement with TG measurements on Ca doped $RE_2Sn_2O_7$ (RE = La, Sm, Er), that showed an increase in the water uptake (at a given temperature) and a more exothermic hydration enthalpy with increasing RE ion size. Moreover, the DFT calculations showed that systems with large X site ions, such as cerates, are predicted to behave as disordered systems with defect formation occurring among the different oxygen sites; whereas systems with smaller X site ion behave as ordered pyrochlores with defect formation occurring on the O48f sites.

Traditionally the enhancement of ionic conductivity is achieved by acceptor doping. Yet, compounds without acceptor doping, and with inherently defective disordered structures are found to exhibit comparable levels of ionic conductivity. Our study in manuscript II showed that $La_2Ce_2O_7$ has a disordered, oxygen deficient, fluorite crystal structure acting effectively as 50% La-doped CeO_2. The electrochemical characterization by means of impedance spectroscopy in the temperature range 1000-200 °C and as a function of water vapour and oxygen partial pressure showed that oxide ion conductivity dominates at high temperatures, while protons are the main charge carrier at temperatures below approximately 450 °C. Moreover, based on the derived defect chemical model it was found that $La_2Ce_2O_7$ may fill all its oxygen vacancies, 1 out of 8 sites, with water, all the way down to room temperature, replacing the positive charge by protons.

We continued our studies on disordered systems and in manuscript III. There, we investigated the influence of order/disorder on the on the ionic conductivity and hydration enthalpy in undoped and acceptor, Ca^{2+}, doped fluorite and pyrochlore structured lanthanum cerate-zirconate oxides. Our study revealed that, the contribution from the ionic conductivity increases and the hydration enthalpy becomes more exothermic with increasing disorder. Moreover, it was found that the ionic conductivity decreases upon

acceptor substitution of La^{3+} with Ca^{2+}. This was interpreted to reflect trapping of the mobile ions by the acceptor Ca'_{La}.

A common characteristic of the above mentioned systems is the negligible grain boundary resistance. As we show in the discussion part of this thesis by exemplifying $La_2Ce_2O_7$, the negligible grain boundary resistance is attributed to the low $\Delta\phi$ and λ^* of the system, stemming from the high acceptor doping level.

Coming to the electrodics part of this thesis, in manuscript IV, we discussed the influence of the incorporation of the ionic phase on the cathode performance. We tested composite cathodes of La_2NiO_4 and $La_{5.6}WO_{11.4}$ in different ratios, using $La_{5.6}WO_{11.4}$ as the electrolyte. The cathode with the single phase La_2NiO_4 and the cathode with 50 wt.% La_2NiO_4 revealed comparable to each other, polarization resistance, and for the composite cathode with 50 wt.% La_2NiO_4 we elucidated the rate determining step.

Concluding this thesis and addressing the main findings; in the first manuscript we found that the hydration thermodynamics of $RE_2X_2O_7$ (RE = La-Lu and X = Ti, Sn, Zr and Ce) series depend on the RE ion radii, and that the formation of oxygen vacancies on the 8*b* site and oxygen interstitials on the 8*a* is also favorable, in addition to the vacancies at the 48*f* site when substituting Zr^{4+} with Ce^{4+}, cf. Fig.6.1. The latter helped us to explicate the effect of cation order/disorder on the hydration thermodynamics and ionic conductivity on lanthanum cerate-zirconate based compounds in manuscript III, where we found that increasing cation disorder favors the hydration and the ionic conductivity of the studied systems, cf. Fig.6.2.

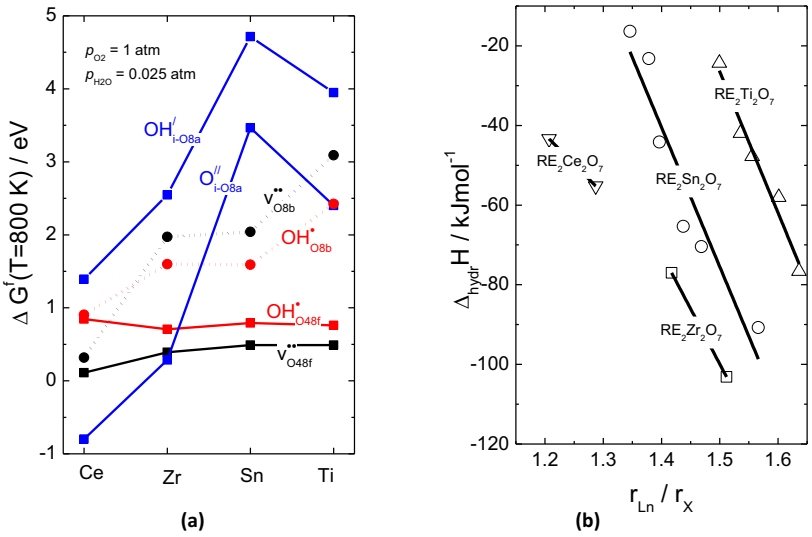

Figure 6.1 (a) Hydration enthalpies versus the r_{RE}/r_X ratio of $RE_2X_2O_7$ (X=Ti, Sn, Zr, Ce) series (b) Equilibrium defect formation energies in the series $Sm_2X_2O_7$ (X=Ti, Sn, Zr, Ce) at 800 K, p_{H_2O}=0.025 and p_{O_2}=1 atm as obtained when solving the electroneutrality with $\left[Ca'_{RE}\right] = 0.01$ mole fractions.

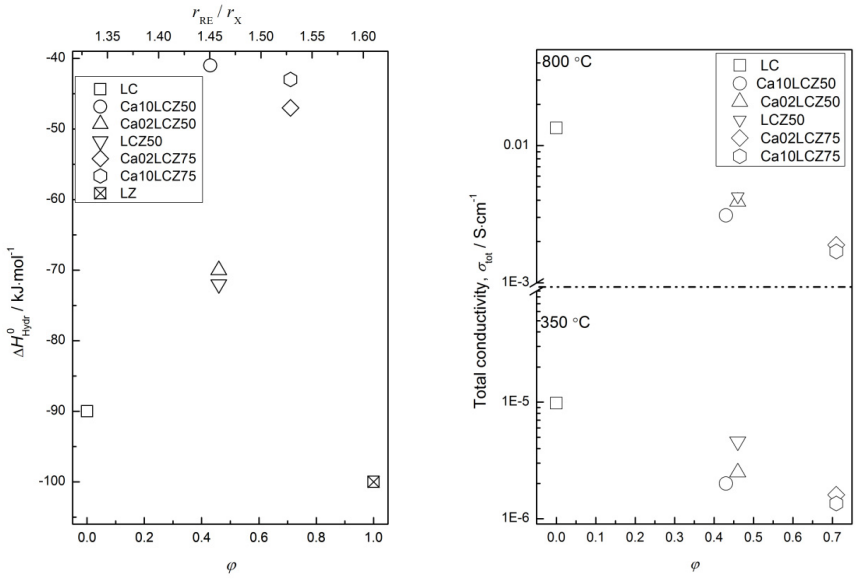

(a) **(b)**

Figure 6.2 (a) Hydration enthalpy, ΔH^0_{Hydr} determined from TG-DSC measurements for $(La_{1-y}Ca_y)_2(Ce_{1-x}Zr_x)_2O_{7-\delta}$ (y=0, 0.02, 0.10 and x=0, 0.50, 0.75), *vs.* cation order factor φ and r_{RE}/r_X (b) Total conductivity of $(La_{1-y}Ca_y)_2(Ce_{1-x}Zr_x)_2O_{7-\delta}$ (y=0, 0.02, 0.10 and x=0, 0.50, 0.75)*vs.* cation order factor φ at 800 °C (dominating oxide ion conductivity) and 350 °C (dominating proton conductivity) under wet O_2, p_{H_2O}= 0.025 atm.

In manuscript II, based on room temperature neutron and powder X-ray diffraction we found that the average crystal structure of $La_2Ce_2O_7$ is well described as disordered fluorite. Moreover, we developed a defect chemical model founded in thermogravimetry and conductivity data, and derived the thermodynamic and transport parameters of the system, cf. table 6.1

Table 6.1 Thermodynamic and transport parameters extracted from modelling of partial and total conductivity data, and from TG and TG-DSC measurements

ΔS^0_{Hyd}	ΔH^0_{Hyd}	u_{0,H^+}	$\Delta H_{m,H^+}$	$u_{0,O^{2-}}$	$\Delta H_{m,O^{2-}}$
[J·mol^{-1}·K^{-1}]	[kJ·mol^{-1}]	[cm^2·K·V^{-1}·s^{-1}]	[kJ·mol^{-1}]	[cm^2·K·V^{-1}·s^{-1}]	[kJ·mol^{-1}]
-125 ± 12	-93 ± 12	113 ± 7	81 ± 3	5000 ± 800	108 ± 2

Finally, in manuscript IV we found that, the incorporation of the ionic phase in the cathode did not decrease but instead increases area specific polarization resistance. This was explained by the loss of MIEC surface area in the composite cathode as compared with the single phase cathode. Moreover, our analysis on the rate determining step for the composite cathode with 50 wt% ionic phase, revealed that the process related to dissociative adsorption of O_2 had the highest activation energy.

Appendix

EFFIPRO summary

This work has been part of the EFFIPRO project: ***EFFI****cient and robust cell with novel ceramic* ***PRO****ton conducting electrolyte*, funded by the European Union FP7. EEFIPRO explored the use of novel Sr- and Ba-free stable oxides that may make an efficient PC-SOFC also robust. It took as starting point the discovery at University of Oslo (UiO) in 2004 of Ca-doped $LaNbO_4$ (LCN) [58] as the best among a new class of stable but modest proton conductors [43], which require novel electrodes and fabrication of thin film electrolytes. The aim was not to assemble a complete cell, rather to reach quantifiable goals of electrolyte thickness, conductivity, and electrode polarisation of support-anode-electrolyte and cathode-electrolyte assemblies. During the course of the project, it became clear that LCN or other $LaNbO_4$ class formulations could not be brought to the targeted conductivity, and could not sustain cathodes anywhere near to the set targets of the project. At midterm they were replaced with the emerging "$La_{6-x}WO_{12-3x/2}$" (LWO) class of proton conducting oxides. LWO was found to be most stable, also in CO_2, with proton conductivity of 0.0015 S/cm satisfying final target.

LWO reacts with NiO and for that reason EFFIPRO investigated Sr-doped $LaCrO_3$ as barrier and functional anode. A 2.5 μm LWO electrolyte was made by pulsed layer deposition (PLD) on a porous LSC layer spray-deposited on an alloy support, the first so-called 3rd generation PC-SOFC structure reported. Other developments included Ni post sintering infiltration and reductive precipitation of catalytic Ni nanoparticles from Ni-substituted LSC. As cathode for LWO we investigated substituted, infiltrated, and nanostructured $LaMnO_3$ and La_2NiO_4 as well as the fundamentals of $La_2Ce_2O_7$ as mixed conducting electrode component.

EFFIPRO counts 7 partners in 5 countries coordinated by UiO (cf. Table A1). It has met the majority of its milestone targets and at closure lists 1 patent, 11 articles, and 26 presentations. It has led to several follow-up projects to make PC-SOFC an effective alternative for the emerging hydrogen economy.

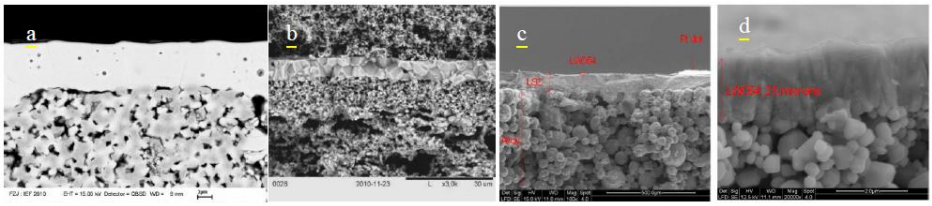

Figure A1. a) 7 µm LCN on Ni_LCN cermet b) LCN between supported functional anode and cathode c) 3rd generation PC-SOFC; coarse alloy support, fine LSC anode and thin dense LWO (hardly visible) d) close-up of the same LWO on LSC.

Table A1. List of EFFIPRO partners.

Partner name	abbreviation	Country
University of Oslo	UiO	Norway
Centre National de la Recherche Scientifique; Institut des Matériaux Jean Rouxel, IMN	CNRS	France
Inst. Chemical Technology, U.P. Valencia/CSIC	CSIC-ITQ	Spain
SINTEF	SINTEF	Norway
Forschungszentrum Jülich	JÜLICH	Germany
Fuel Cells and Solid State Chemistry Department, Risø National Laboratory for Sustainable Energy, Tecnical University of Denmark	RISØ-DTU	Denmark
Ceramic Powder Technology AS	CERPOTECH	Norway

Substrate/anode/electrolyte

An objective of EFFIPRO is to develop a stable, thin anode-supported proton conducting electrolyte. The goals at midterm were 5 μm electrolyte with area specific (ASR) of 0.5 Ωcm^2 and an anode polarization ASR of 0.5 Ωcm^2, both in wet H_2 at 800 °C. Target at the end of the project was to have a 3 μm electrolyte with ASR of 0.2 Ωcm^2 and an electrochemical anode ASR of 0.2 Ωcm^2 at 700 °C. The electronic conductivity of the anode material should surpass 100 S/cm at midterm and 200 S/cm at the end of the project. The work has been done between three partners that offer partly complementary and partly overlapping technologies and were assigned three different routes – partly complementary and partly overlapping but most of all focusing on the different layers that make up the half-cell.

Substrate/anode/LWO electrolyte

At midterm when EFFIPRO changed electrolyte material from LCN to LWO the development of substrate, anode, and cathode started from scratch. $La_{1-x}Sr_xCrO_3$ (LSCO) was chosen as candidate anode functional layer between the Ni in the cermet and the LWO, as they are known to react. The options were narrowed down from the work on LCN in order to succeed making LWO-based systems in the remaining time. JÜLICH would use standard Ni-YSZ SOFC substrates instead of developing new ones for LWO, since the LSC layer would in any case come in between. SINTEF would deposit LSC and LWO on anode-alloy substrate. RISØ-DTU would contribute with LWO electrolyte film deposition on JÜLICH and SINTEF anodes, and with testing them. Finally, UiO would assisted with its pulsed layer deposition (PLD) facility to study the effect of the inclusion of a 400 nm dense film of LSCO on the performance of Ni-LSCO anode on LWO, and to make sufficiently thin functional electrolyte for the final tests.

The work at JÜLICH showed that it was difficult to sinter a dense electrolyte on top of LSCO which was, in turn, on top of a Ni-YSZ cermet, without delamination or reaction between materials. This is caused by the high temperature needed for sintering and the consequent high cation inter-diffusion between and through the layers, possibly also over surfaces in the porous components. It was finally concluded that anodes based on Ni and LWO would have to be made by making dense LWO on a porous LWO substrate and

thereafter infiltrating the porous with Ni-containing solution, which after reduction during operation as anode becomes metallic. This was carried out by RISØ-DTU; after reduction to Ni and application of gold counter electrode they measured an electrolyte resistance in correspondence with the conductivity of the 30 μm thick LWO electrolyte layer.

SINTEF focused on investigation of robust manufacturing routes for porous alloy substrates and compatible functional anodes with reduced cost. These layers are integrated in the 3rd generation alloy supported fuel cells. From the different routes, tape-casting was selected for producing porous substrates of ferritic alloys. Flat alloy substrates 1 mm thick were successfully obtained with connected porous networks after single casting and annealing step.

The anode functional layer (LSCO or Ni-LSCO) was then applied by spray-coating. Suspensions and parameters were optimized to avoid infiltration of LSCO grains into the metallic substrates, to improve adhesion and to provide a suitable surface for the deposition of the electrolyte layer. The application of LWO layer was investigated through three main paths using spray-coating, electrophoretic deposition in collaboration with RISØ-DTU, and PLD in collaboration with UiO.

The deposited LWO layers by electrophoretic deposition were homogenous and well adhered to the anode/substrate assembly. However, the layers remained porous and it was not possible to sinter the cells at higher temperatures than 1350 °C due to melting of the alloy. Deposition of LWO layers by spray-coating resulted similar outcomes.

In UiO the PLD enabled us to produce thin dense electrolyte layers of around 3 microns on the alloy/LSCO substrate after adjustment of the substrate temperature and atmosphere in the PLD chamber (cf. Fig. A2). This electrolyte thickness reaches one of the final targets of the project. Post annealing did not cause microstructural changes, and the electrolyte remained crack-free. Testing of the cells was conducted at UiO on the PLD deposited LWO layers coated on LSCO/alloy substrates, which were post anneal at 700 and 800 °C for 24 h. The cell was characterized by EIS from 500 to 700 °C in wet 5% H_2 in Ar. The ASR of the electrolyte was 1.2 $\Omega \cdot cm^2$ at 700 °C, and the activation energy was approximately 0.5 eV.

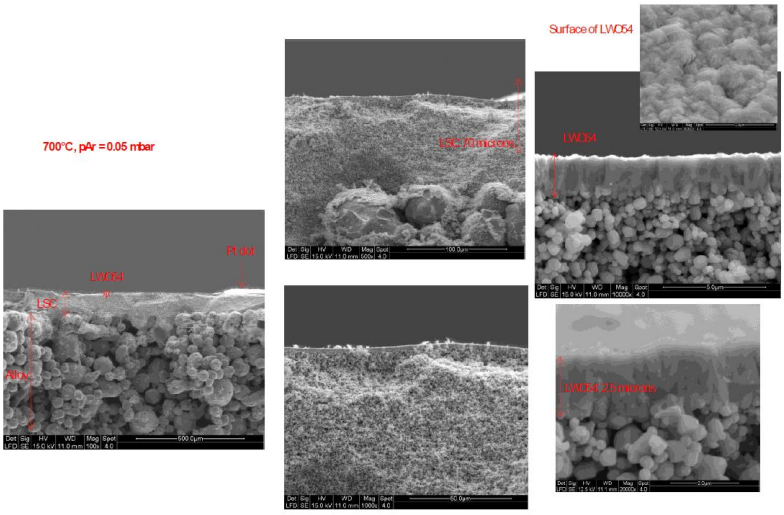

Figure A2. Left: SEM micrograph of the entire anode-substrate structure, with coarse porous alloy, finer porous LSCO, and dense thin (hardly visible) LWO. Middle: close-ups of alloy-LSCO interface (top) and LSCO+LWO (bottom). Right: Further close-ups of the porous LSCO and dense LWO.

Ni-LSCO / LWO interface

In a parallel activity UiO investigated the interface between Ni-LSCO and LWO. Namely in UiO we studied the effect of the inclusion, by PLD, of a 400 nm dense film of LSCO between Ni-LSCO and LWO on the performance of Ni-LSCO anode. The effect was studied both on a $La_{5.6}WO_{11.4}$ (LWO56) and a $La_{5.4}WO_{11.2}$ (LWO54) electrolyte. The electrochemical characterization of the system was performed by means of EIS in the temperature range 900-700 °C in a three electrode configuration (cf. Fig. A3) under 5 % wet H_2 in Ar.

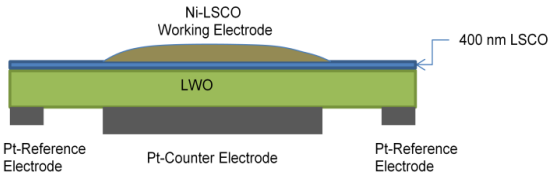

Figure A3. Illustration of the three electrode configuration used in the experiment. For current collection at the working electrode, Pt paste and Pt net were used. The reference and counter electrodes were Pt paste.

Fig. A4.a depicts the cross section of Ni-LSCO/LSCO film/LWO(56), analyzed by SEM after the electrochemical characterization. From the SEM micrograph the adhesion between the LWO(56) and the dense LSCO film can be assessed. Moreover the line scan (EDXS; EDAX Pegasus 2200) in Fig.A4.b taken at the contact point between Ni grain/LSCO film/LWO(56) suggests that there is no reaction between the LSCO film and the LWO(56). Furthermore, the intensification of the Cr signal approx. 360 nm before the Ni signal, confirms the thickness of the LSCO film.

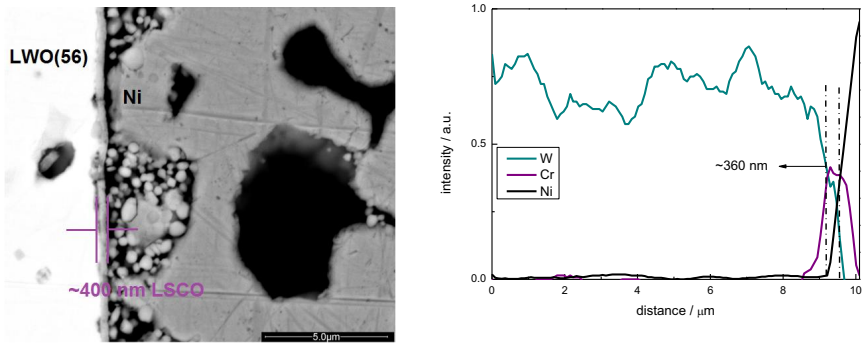

(a) **(b)**

Figure A4. a) SEM micrograph of the cross section of the sample after measurement and b) line scan of at the contact point between the Ni-LSCO/LSCO film/LWO(56). From the intensity of the signals the thickness of the LSCO film can be seen.

For sake of comparison, a cell without the inclusion of the 400 nm dense film of LSCO was also tested. Fig. A5.a depicts the cross sections of that cell after the electrochemical characterization. No obvious signs of electrode delamination can be observed, and the good adherence between the anode and the electrolyte is evident; without any noticeable

signs of reaction between Ni or LSCO with LWO(56). The latter is further supported from the line scan in Fig A5b.

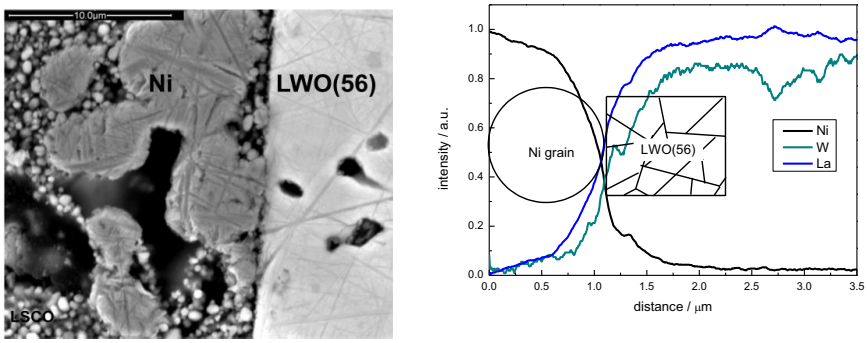

(a) **(b)**

Figure A5. a) SEM micrograph of the cross section of the sample after measurement and b) line scan of the Ni-LSCO/LWO(56) interface. For sake of illustration we graphically portray the contact between a Ni grain and the LWO(56) surface.

Fig. A6 compares the polarization resistance of the two cells as a function of temperature in wet 5% H_2 in Ar. The Ni-LSCO/LSCO film/LWO(56) exhibits a lower polarization resistance and somewhat lower activation energy than the Ni-LSCO/LWO(56).

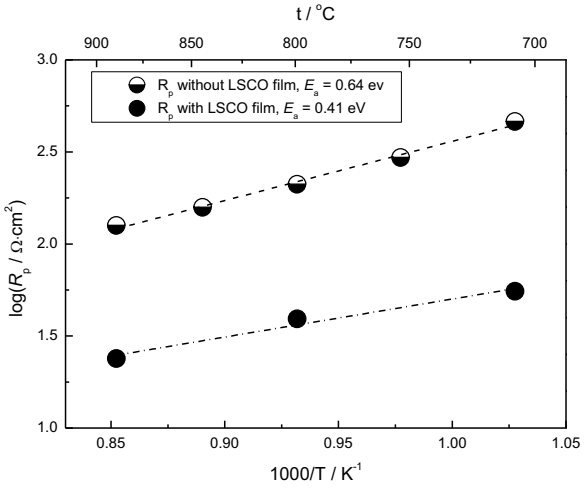

Figure A6. Polarization resistance Ni-LSCO/LWO(56) with and without the 400 nm thick LSCO film as a function of inverse temperature in wet 5 %H_2 in Ar.

Fig. A7 shows the temperature dependence of the apparent electrolyte resistivity as a function of temperature for the two different cells. The inclusion of the LSCO film results a decrease of the apparent electrolyte resistivity. The observed activation energies for the two systems are to some extent in the same range. As the electrolyte for the two systems is identical the decrease of the apparent electrolyte resistivity can be explained by an improvement in the contact between electrolyte and electrode, when the LSCO film is included [59-61].

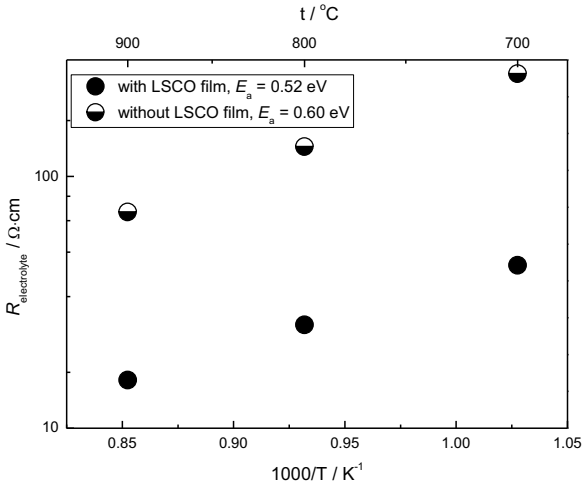

Figure A7. Electrolyte resistivity as a function of temperature in wet HArmix.

We performed the same study also for LWO (54). In order to reduce the Ni grain size which would in turn facilitate the catalytic activity of Ni towards H_2, we reduced the annealing temperature of the anode under H_2 from 1200 °C to 1150 °C. A fracture from such a cell after measurement is shown in Fig. A8. The Ni grain size is clearly reduced (compare Fig. A4a with A8), the anode adherence is visibly in order, the porosity appears to be adequate for gas diffusion, and from the plot in Fig. A9 the polarization resistance appears to be largely reduced compared for the anode annealed at 1150 °C.

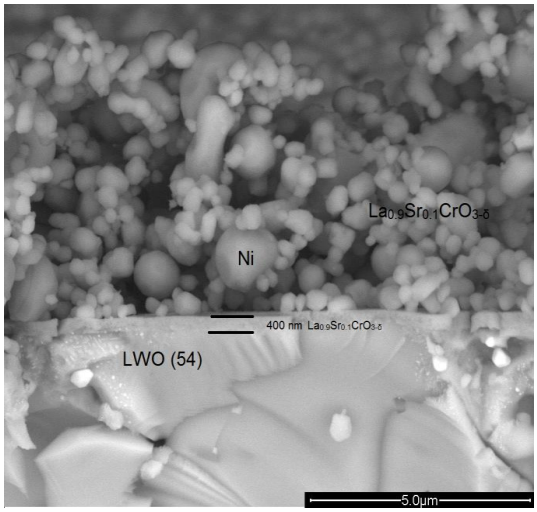

Figure A8. Fracture after measurement of the cell with anode annealed at 1150 °C under HArmix for 5 h.

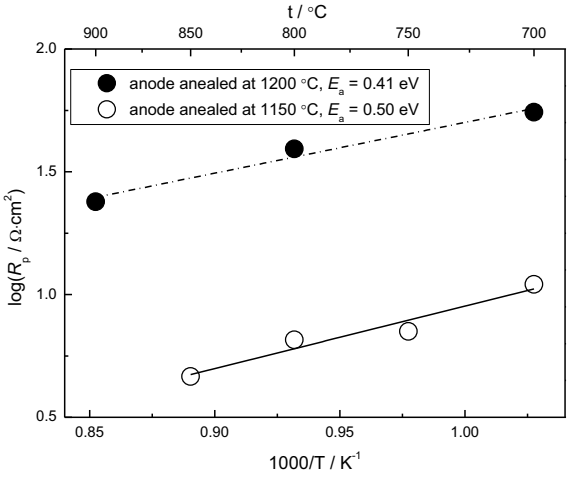

Figure A9. Comparison of the polarization resistance as a function of temperature for the anode annealed at 1200 °C (closed circles) and the anode annealed at 1150 °C (open circles).

References for chapters 1-3,5,6, and Appendix.

[1] Aristotle, D. Bostock, *Metaphysics, Book Z-H*, Clarendon Press, Oxford (1994).

[2] P. Atkins, J.D. Paula, *Atkins' Physical Chemistry*, Oxford University Press, Oxford (2006).

[3] R.E. Smalley, *MRS Bulletin* **30** (2005) (6) 412.

[4] K.R. Webb, *Journal of the Royal Institute of Chemistry* **85** (1961) (August) 291.

[5] http://www.bloomenergy.com/about/company-history/.

[6] R. Peng, T. Wu, W. Liu, X. Liu, G. Meng, *Journal of Materials Chemistry* **20** (2010) (30) 6218.

[7] E. Fabbri, S. Licoccia, E. Traversa, E. D. Wachsman,, *Fuel Cells* **9** (2009) (2) 128.

[8] A. Grimaud, F. Mauvy, J. Marc Bassat, S. Fourcade, M. Marrony, J. Claude Grenier, *Journal of Materials Chemistry* **22** (2012) (31) 16017.

[9] A. Grimaud, F. Mauvy, J.M. Bassat, S. Fourcade, L. Rocheron, M. Marrony, J.C. Grenier, *J. Electrochem. Soc.* **159** (2012) (6) B683.

[10] S.W. Tao, Q.Y. Wu, D.K. Peng, G.Y. Meng, *Journal of Applied Electrochemistry* **30** (2000) (2) 153.

[11] A.R. Cleave, Atomic Scale Simulations for Waste Form Applications, *Department of Materials*, Imperial College of Science, London (2006).

[12] K. Momma, F. Izumi, *Journal of Applied Crystallography* **41** (2008) (3) 653.

[13] C. Stanek, PhD Thesis, Imperial College of Science, London (2003).

[14] P.K. Moon, PhD Thesis, Massachusetts Institute of Technology, Cambridge (1988).

[15] J.A. Díaz-Guillén, M.R. Díaz-Guillén, K.P. Padmasree, A.F. Fuentes, J. Santamaría, C. León, *Solid State Ionics* **179** (2008) (38) 2160.

[16] L. Cai, A.L. Arias, J.C. Nino, *Journal of Materials Chemistry* **21** (2011) (11) 3611.

[17] P.J. Wilde, C.R.A. Catlow, *Solid State Ionics* **112** (1998) (3-4) 173.

[18] W.W. Barker, P.S. White, O. Knop, *Canadian Journal of Chemistry* **54** (1976) (14) 2316.

[19] T. Norby, *Defects and transport in crystalline solids* University of Oslo (2009).

[20] T. Norby, in: T. Ishihara, Editor, Springer US (2009), p.217-241.

[21] L. Minervini, R. W. Grimes, K. E. Sickafus, *Journal of the American Ceramic Society* **83** (2000) (8) 1873.

[22] L. Minervini, R.W. Grimes, Y. Tabira, R.L. Withers, K.E. Sickafus, *Philos. Mag. A-Phys. Condens. Matter Struct. Defect Mech. Prop.* **82** (2002) (1) 123.

[23] N. Bonanos, *Solid State Ionics* **145** (2001) (1-4) 265.

[24] T. Norby, M. Widerøe, R. Glockner, Y. Larring, *Dalton Trans.* (2004) 3012.

[25] M. Born, R. Oppenheimer, *Annalen der Physik* **389** (1927) (20) 457.

[26] P. Hohenberg, W. Kohn, *Physical Review* **136** (1964) (3B) B864.

[27] W. Kohn, L.J. Sham, *Physical Review* **140** (1965) (4A) A1133.

[28] J. Nyman, PhD Thesis, Chalmers University of Technology, Gothenburg (2012).

[29] M.W. Chase, NIST-JANAF Thermochemical Tables, The American Institute of Physics for the National Institute of Standards and Technology, New York (1998).

[30] H. Uchida, S. Tanaka, H. Iwahara, *Journal of Applied Electrochemistry* **15** (1985) (1) 93.

[31] W. Zhou, R. Ran, Z. Shao, *Journal of Power Sources* **192** (2009) (2) 231.

[32] B. Lin, Y.C. Dong, R.Q. Yan, S.Q. Zhang, M.J. Hu, Y. Zhou, G.Y. Meng, *Journal of Power Sources* **186** (2009) (2) 446.

[33] L. Zhao, B. He, B. Lin, H. Ding, S. Wang, Y. Ling, R. Peng, G. Meng, X. Liu, *Journal of Power Sources* **194** (2009) (2) 835.

[34] W. Jung, H.L. Tuller, *Solid State Ionics* **180** (2009) (11-13) 843.

[35] J.R. Tolchard, H.L. Lein, T. Grande, *Journal of the European Ceramic Society* **29** (2009) (13) 2823.

[36] S.P. Jiang, *Journal of Materials Science* **43** (2008) (21) 6799.

[37] F. He, T. Wu, R. Peng, C. Xia, *Journal of Power Sources* **194** (2009) (1) 263.

[38] S. Yamaguchi, T. Shishido, H. Yugami, S. Yamamoto, S. Hara, *Solid State Ionics* **162–163** (2003) (0) 291.

[39] N. Hildenbrand, PhD Thesis, University of Twente, Enschede (2011).

[40] J.E.B. Randles, *Discussions of the Faraday Society* **1** (1947) (0) 11.

[41] R. Gerhardt, A.S. Nowick, *Journal of the American Ceramic Society* **69** (1986) (9) 641.

[42] X. Guo, W. Sigle, J.U. Fleig, J. Maier, *Solid State Ionics* **154-155** (2002) 555.

[43] R. Haugsrud, T. Norby, *Nat Mater* **5** (2006) (3) 193.

[44] K.D. Kreuer, *Solid State Ionics* **125** (1999) (1) 285.

[45] H.G. Bohn, T. Schober, *Journal of the American Ceramic Society* **83** (2000) (4) 768.

[46] C. Kjølseth, H. Fjeld, Ø. Prytz, P.I. Dahl, C. Estournès, R. Haugsrud, T. Norby, *Solid State Ionics* **181** (2010) (5-7) 268.

[47] S.M. Haile, D.L. West, J. Campbell, *Journal of Materials Research* **13** (1998) (6) 1576.

[48] R.A. De Souza, Z.A. Munir, S. Kim, M. Martin, *Solid State Ionics* **196** (2011) (1) 1.

[49] K.D. Kreuer, *Ann. Rev. Mater. Res.* **33** (2003) 333.

[50] T. Norby, *Solid State Ionics* **125** (1999) (1-4) 1.

[51] H. Iwahara, T. Esaka, H. Uchida, N. Maeda, *Solid State Ionics* **3-4** (1981) (C) 359.

[52] K.B. Kostøl, A. Magrasó, T. Norby, *International Journal of Hydrogen Energy* **37** (2012) (9) 7970.

[53] X. Guo, R. Waser, *Progress in Materials Science* **51** (2006) (2) 151.

[54] R.A. De Souza, *Physical Chemistry Chemical Physics* **11** (2009) (43) 9939.

[55] X. Guo, W. Sigle, J. Maier, *Journal of the American Ceramic Society* **86** (2003) (1) 77.

[56] N. Armaroli, V. Balzani, *Angewandte Chemie - International Edition* **46** (2007) (1-2) 52.

[57] V. Smil, *World Watch* **19** (2006) (1) 22.

[58] R. Haugsrud, T. Norby, *Solid State Ionics* **177** (2006) (13-14) 1129.

[59] N. Hildenbrand, B.A. Boukamp, P. Nammensma, D.H.A. Blank, *Solid State Ionics* **192** (2011) (1) 12.

[60] J.I. Gazzarri, O. Kesler, *Journal of Power Sources* **167** (2007) (1) 100.

[61] J.I. Gazzarri, O. Kesler, *Journal of Power Sources* **167** (2007) (2) 430.

Acknowledgments

Finally, the acknowledgments, the part that everyone who is receiving this book will *definitely* be reading.

What a *journey*! More than 3.5 years with emotions following the course of a rollercoaster. However, the foundations for this journey that started in 2009 were set few years ago, back in 2005. I will come to this later in the text, so let me take things chronologically starting from today.

Firstly, I would like to thank my two supervisors Prof. Truls Norby and Assoc. Prof. Reidar Haugsrud. Truls thank you very much for trusting me and giving me the task to carry out the work that the EFFIPRO project demanded. Your enthusiasm, endurance, and *pure love* for science have been great motivations for me. Reidar thank you very much for being so supportive and available any time of the day, especially these last months when late evenings were my only option; your constructive criticism and encouragement has been so vital. Moreover, I would like to thank both for your sound guidance; your scientific knowledge and demand for quality brought me to a level far greater than I would anticipate.

Furthermore, I would like to thank all my colleagues/friends from the group of Solid-State Electrochemistry for welcoming me and creating a joyful, memorable, and inspiring working environment. In particular, I would like to thank Harald Fjeld and Wen Xing- who during my first months in the group were a great source of information and guidance in the lab, Einar Vøllestad- for being a great officemate, Tor S. Bjørheim- for the fruitful discussions, great input on pyrochlores and fun ski trips, Anders Werner Bredvei Skilbred- for being a fantastic friend in and out the group, great companion on our "expeditions" in the mountains and bike trips, Ragnar Strandbakke- for being a great friend, great support on the understanding of cathodes, and helping to do the impossible possible.

Outside the research group I would like to thank Assoc. Prof. Christopher Knee and Dr. Istaq Ahmed for their excellent collaboration during the writing of manuscript II. Moreover, I would like to thank Dr. Sandrine Ricote for her significant input in manuscript III; Sandrine your positivism has been a great drive for me.

Coming to 2005, I could not foresee at that point, when my two supervisors at that time and good friends now, Asst. Prof George Marnellos and Lecturer Costas Athanasiou encouraged me to move to The Netherlands and pursue a Master's degree, that today I would write these lines. I am deeply thankful to both for showing me the path, and the support whenever I was in need for.

Coming to the Netherlands I was fortuned to meet Dr. Bernard Boukamp together with Dr. Nicolas Hildenbrand (PhD student at that time). Their enthusiasm and deep understanding of science helped me to build the basis and stamina for the demanding, to say the least, task of pursuing a PhD. Thank you both.

Further I would like to express my deep gratitude to my mom and sister, for believing in me and *letting me go* to follow my dreams the *time* they needed me the most. Allow me to express these few words in my mother tongue. *Μανα μου* και *αδερφή μου* σας ευχαριστώ από τα βάθη της καρδίας μου για την αμέριστη υποστήριξη όλα αυτά τα χρόνια, είμαι ότι είμαι χάρη στην συμπαρασταση σας.

Finally coming to *Siri*. You have been with me since day one, being fondly on the tough times and encouraging on the pleasant times. Thank you for your selfless support all these years is the least I can say.